Correspondence to harde@hsu-hh.de
Vol. 2.1 (2022)
pp. 1-33

Verification of the Greenhouse Effect in the Laboratory

Hermann Harde[1], Michael Schnell[2]

[1]Helmut-Schmidt-University, Hamburg, Germany

[2]Ex Academy of Science of GDR, Berlin, Germany

Abstract

The existence or non-existence of the so-called atmospheric greenhouse effect continuously dominates the extremely emotional discussion about a human impact on global warming. Most scientists agree with the fundamental greenhouse theory, but like their opponents they are missing a reliable experimental verification of this effect. Measurements at the open atmosphere are too strongly affected by perturbations to quantify the relatively small contribution of greenhouse gases to local heating of the air or the Earth's surface. Therefore, we have developed an advanced laboratory set-up, which allows to largely eliminate convection or heat conduction and to reproducibly study the direct influence of greenhouse gases under similar conditions as in the lower troposphere. We measure the additional warming of a pre-heated plate due to back-radiation of the greenhouse gases carbon dioxide, methane and nitrous oxide as a function of the gas concentration, and we derive from the observed warming the radiative forcing of these gases. The measurements are well confirmed by radiation transfer calculations and underline that there exists no climate emergency.

Keywords: Greenhouse effect; infrared-active gases; radiative forcing; carbon dioxide, methane; nitrous oxide.

Submitted 01-11-2021, Accepted 16-12-2021. https://doi.org/10.53234/scc202203/10

1. Introduction

The very first explanation of the atmospheric greenhouse effect (GHE) goes back to Jean-Baptiste Joseph Fourier in 1824 [1], who was studying the Earth's energy budget to explain the surface temperature. He was inspired by the hot box of Horace-Bénédict de Saussure consisting of an isolated compartment with several glass windows, which in the inside is strongly heated up by the transmitted solar radiation. Fourier assumed that the atmosphere is acting similar to the glass windows, transparent for the solar radiation but blocking the infrared (IR)-radiation emitted from the ground. Heat exchange with the environment by convection or heat conduction was largely neglected in this model.

First quantitative measurements with IR absorbing gases like water vapor or carbon dioxide (CO_2) go back to Tyndall (1861) [2]. He described the GHE by comparing the atmosphere with a *dam built across a river and causing a local deepening of the stream*; in a similar way should the atmosphere act as a barrier to radiation from the Earth, thus, producing a heightening of the temperature at the Earth's surface. Although he could study the absorptive and emitting behavior of these gases, he had no direct evidence for a GHE.

Within the second half of the 19th century fundamental relations for the interaction of radiation with matter were formulated, e.g., Kirchhoff's law of thermal radiation (1859) [3], the Stefan-Boltzmann law (1879) [4, 5] or Planck's radiation law (1900) [6], which form the theoretical basis of the GHE. First calculations with a still strongly simplified climate model go back to S.

Arrhenius (1898) [7], who already considered ice-albedo feedback in his model and found a CO_2 climate sensitivity (temperature increase at doubled CO_2 concentration) of 5 - 6°C. Since this time there existed continuous trials to confirm or to refute the GHE by more or less simple laboratory experiments. Direct measurements at the atmosphere are too strongly affected by convection, turbulence or scattering effects to quantify the relatively small contribution of greenhouse molecules to any local warming of the air or the Earth's surface.

One of the frontier experimental investigations was performed by R. W. Wood (1909) [8], who used two boxes containing regular air. One box was covered with a glass window transparent for sun light, but blocking IR-radiation, the other covered with a NaCl window transparent also for IR. His measurements showed significant warming of the interior but no or only a negligible temperature difference between the boxes. From this Wood and other author repeating his experiment (e.g., Nahle 2011 [9]) concluded that infrared radiation, which can escape through the NaCl window, will not contribute to heating or only with an insignificant amount, while the observed temperature increase in both boxes - different to Fourier's interpretation - is exclusively explained due to the blockage of convective heat transfer with the environment and not related to any kind of trapped radiation.

But experiments recording the temperature at the floor and ceiling of the interior, rather than looking only to a single temperature for each box, measure a 5°C larger floor to ceiling decline for the salt rock box than the glass box, while the bottom of the boxes have almost identical temperatures (V. R. Pratt 2020 [10]). These results are principally confirmed with a slightly different set-up using an internal electric heating instead of external light sources (E. Loock 2008 [11]). Such heating avoids differences in the incident radiation, which otherwise has to transmit windows of different materials and losses. A higher temperature of 2.5 - 3°C could be found for the glass box, and replacing the glass by a polished aluminum foil the temperature even rises by additional ≈ 3°C.

While the Wood-type experiments can answer the question, if and how far a reduced IR-transmissivity can contribute to warming of a compartment, respectively the troposphere, it gives no information about the interaction of greenhouse gases with IR-radiation. Thus, it still remained the question, to which extent such gases at least partially can withhold IR-radiation and how far simple absorption by GH-gases or the highly disputed back-radiation might contribute to additional warming of the floor. Such studies require to fill one compartment with the gas to be investigated and to compare this with a reference measurement using air or a noble gas.

Meanwhile different approaches have been carried out, partly with external irradiation or with internal heating (see, e.g., Loock [11]), partly measuring the gas temperature or the IR radiation in forward and backward direction (Seim & Olsen 2020 [12]). But either no warming was detected or, after closer inspection, the observed temperature increase could not be attributed to an IR-radiation effect.

Unfortunately, some fake demonstrations with apparent temperature differences of more than 10°C are presented in the internet, which allegedly reveal the strong impact of the greenhouse gases (see, e.g., Ditfurth 1978 [13]. However, closer inspection shows that the higher temperature is mainly caused by a stratification effect combined with an increased isolation, when heavier CO_2 is filled from the bottom into the compartment (M. Schnell 2020 [14]). And really problematic is, when the co-recipient of the 2007 Nobel Peace Prize initiates a web-based campaign with multiple advertisements on television, focused on spreading awareness for a climate crisis and as "evidence" presents a completely unrealistic and unreproducible video experiment of the GHE (Al Gore's Climate 101 video experiment, 2001 [15]), which meanwhile has been falsified by several revisions (A. Watts 2011 [16]; J.-E. Solheim 2016 [17]). It is a dirty propaganda using such a manipulated experiment to spread fear around the word and to indoctrinate our society with the message that we can only rescue our Earth by stopping all future emissions of greenhouse gases. This undermines any serious attempts to discuss and analyze the expected influence of GH-gases on our climate. Political imaginations, speculations or religious faith are no serious

consultants to ensure a prosperous future, our knowledge and technical progress is based on scientific principles.

Therefore, it is time to stop the endless speculations about the disastrous implications of an atmospheric GHE and to concentrate on reliable investigations, which allow to quantify the size and limiting impact of GH-gases on global warming caused by anthropogenic emissions of fossil fuels.

In this contribution we present an advanced experimental set-up, which to a large extent allows to eliminate convection or heat conduction and to reproducibly study the direct influence of greenhouse gases under similar conditions as in the lower troposphere. In Section 2 we present the set-up, which different to other experiments uses a heated plate as radiation source and simultaneously as sensitive detector for the back-radiation from GH-gases. We measure the increasing temperature of this plate or, alternatively at stabilized temperature, the energy saving due to the back-radiation. Section 3 describes the theoretical concept for analyzing and evaluating the experiments. Section 4 contains some preliminary studies for the validation and calibration of the measuring system, and Section 5 presents our measurements together with an evaluation of the data, from which the radiative forcing of the gases CO_2, CH_4 and N_2O can be derived. Our results are discussed in Section 6 and Section 7 gives a summary with future perspectives.

2. Experimental Set-Up

For our studies we use an experimental set-up, which consists of two plates in a closed housing, one plate heated to 30°C, the other cooled to -11.4°C (Fig. 1). The plates have a distance of 1.11 m to each other, and the tank can be filled with different gases to study the radiation transfer between the plates in the presence of the GH-gases.

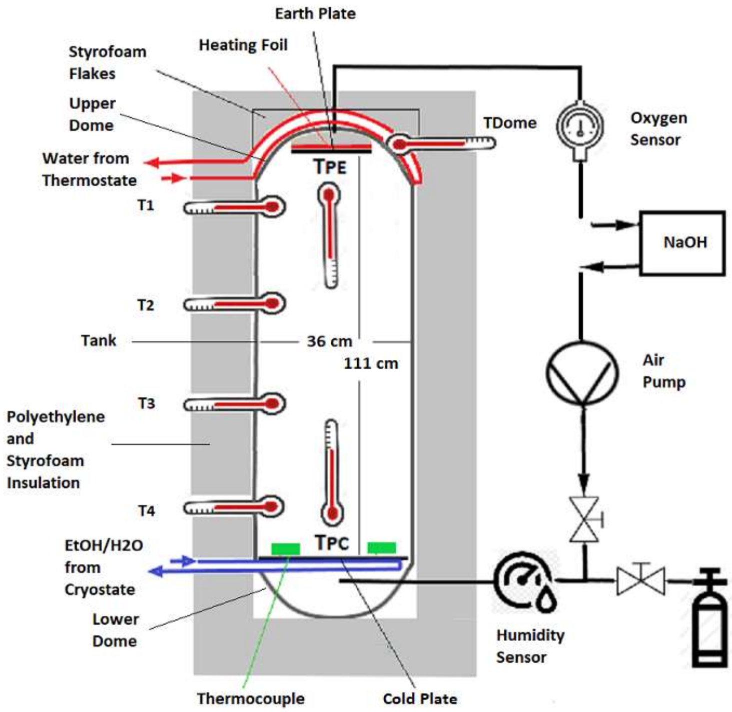


Figure 1: Schematic of the experiment set-up.

Different to other experiments, no light sources from visible to mid IR are used, only the radiation emitted by the two plates and interacting with the gases is considered. This simulates conditions for the radiation exchange similar to the Earth-Atmosphere-System (EASy) with the warmer Earth's surface and the colder atmosphere. It also avoids any problems caused by an inappropriate

spectral range of an external source, which produces a lot of waste heat in the compartment and the windows, but is not well matched to the absorption bands of the GH-gases, and thus significantly reduces the measurement sensitivity (see also Section 3).

With increasing concentration of the GH-gases the radiation balance between the plates is changing and can sensitively be measured as a further increasing temperature of the warmer plate and/or a further cooling of the cold plate. Here we restrict our investigations on recording the temperature variation of the heated plate as a function of the GH-gas concentration in the tank, or alternatively controlling the electric power required to stabilize the temperature of this plate to 30°. In analogy to a presumed warming of the Earth's surface by the atmospheric GHE we designate the warmer plate as the earth plate, which simultaneously is acting as source and sensor for IR-radiation.

Any flows, which are not part of the radiation exchange must be prevented or minimized by appropriate measures. Fig. 1 shows the schematic set-up and the most important components; for further details, see Appendix 1. Their vertical installation, with the earth plate in the top position, ensures a stable gas stratification during gas injection and prevents vertical heat exchange by convection.

Heat conduction, both along the compartment walls or by the gas, cannot be prevented but minimized. The earth plate is fixed in isolation and located in a hemispheric cover (dome) with almost identical temperature. The dome is wrapped with a vinyl tube on the outside (Appendix 1) and water at a constant temperature of 30.0 ± 0.1°C, controlled by an electric heating, flows through this hose. This arrangement is essential for our investigations and ensures that there is almost no heat conduction in this section. The heated dome guarantees good thermal insulation of the earth plate, but is also an important orientation aid for the evaluation of the experiments. It has a polished stainless-steel surface, which makes it largely insensitive to thermal radiation.

When adding a GH-gas the back-radiation of the gas is measured as increasing temperature of the black colored earth plate relative to the dome temperature, or as reduced electrical power for heating the plate. For the calibration of the different temperature sensors, see Appendix 2.

From the outset, the earth plate together with the dome has the highest temperature. This results in a small, unavoidable heat flow from the earth plate to the tank walls and the cold plate, supported by the gases. Any impact of this heat conduction, which inherently is very small, is checked by control measurements with noble gases of comparable heat conductivity (Appendix 3). The preparation and realization of a measurement together with the data registration system is described in Appendix 1.

3. Theoretical Basis of the Greenhouse-Effect and Data Analysis

In this section we summarize the physical background of IR-radiation interacting with the GH-gases. As example we consider the interaction with CO_2 molecules, this with particular emphasis to the radiation transfer in the gas and the back-radiation to the earth plate. The presented theoretical concept allows to precisely simulate the GHE under the given experimental conditions, and it forms the basis for a quantitative analysis of the measurements.

3.1 Spectral Properties of CO_2

The spectral range relevant for the interaction of longwave (lw) radiation with infrared-active molecules is determined by the Earth's surface temperature, or here, the temperature T_E of the earth plate. The spectral intensity of a black body at temperature T_E (in units of Kelvin) is given by Planck's radiation law [5] as a function of the wavelength λ (in µm):

$$I_\lambda = \frac{2\pi \cdot h \cdot c^2}{(\lambda \cdot 10^{-6})^5} \frac{1}{e^{h \cdot c \cdot 10^6/(k_B \cdot T_E \cdot \lambda)} - 1} \cdot 10^{-6} \left[\mathrm{W/m^2/\mu m}\right], \tag{1a}$$

with $h = 6.626 \cdot 10^{-34}$ Ws^2 as Planck's constant, $c = 2.998 \cdot 10^8$ m/s as vacuum speed of light and

$k_B = 1.381 \cdot 10^{-23}$ J/K as Boltzmann's constant.

In wide areas of spectroscopy, it is more common to present spectroscopic data in reciprocal wavelengths $\tilde{\nu} = 1/\lambda$ and in units of cm^{-1}. This corresponds to a frequency scale $\nu = c/\lambda$, divided by c and is designated as wavenumbers. The respective Planck distribution then takes the form:

$$I_{\tilde{\nu}} = 2\pi \cdot h \cdot c^2 \cdot \tilde{\nu}^3 \frac{1}{e^{h \cdot c \cdot \tilde{\nu} \cdot 100/(k_B \cdot T_E)} - 1} \cdot 10^8 \; \left[\mathrm{W/m^2/cm^{-1}}\right]. \qquad (1b)$$

Fig. 2 shows the emitted spectral intensity (Blue Line) of the earth plate at T_E = 30°C (303.15 K). Within this spectral range CO_2 with its different isotopologues possesses more than 30,000 lines with a spectral line intensity larger 10^{-26} cm/molecule (for definition, see e.g., Rothman et al. 2008 [18]; Harde 2013, Subsec. 2.2.2 [19]), and even the most frequent isotopologue $^{12}C^{16}O_2$ with an abundance of 98.89 % holds 12,400 lines.

By far the strongest absorption band with spectral line intensities up to $3.3 \cdot 10^{-18}$ cm/molecule is centered around 2,400 cm^{-1} ($\lambda \approx 4.25$ µm). But at these wavenumbers the emitted spectral intensity of the earth plate is hundred times smaller than at its maximum. So, this absorption band cannot contribute more than 0.75% to the total absorption. The dominant interaction with rovibronic transitions of the CO_2 bending oscillation happens around $\tilde{\nu} = 670\,\mathrm{cm}^{-1}$ ($\lambda \approx 15$ µm), although the spectral line intensities and thus the respective absorption coefficients are roughly 30x smaller than the stronger lines at 2,400 cm^{-1}. Plotted in Fig. 2 is the calculated spectral intensity transmitting a gas sample of 20% CO_2 in dry air at a constant temperature of 20°C and over a distance of 111 cm (Plum colored). The semi-transparent wings of this absorption band (Gray) together with the weak bands around 1,000 cm^{-1} and 2,100 cm^{-1} are only partly contributing to a further slowly increasing absorption with inclining CO_2 concentration (all concentration specifications in this contribution are relating to the volume).

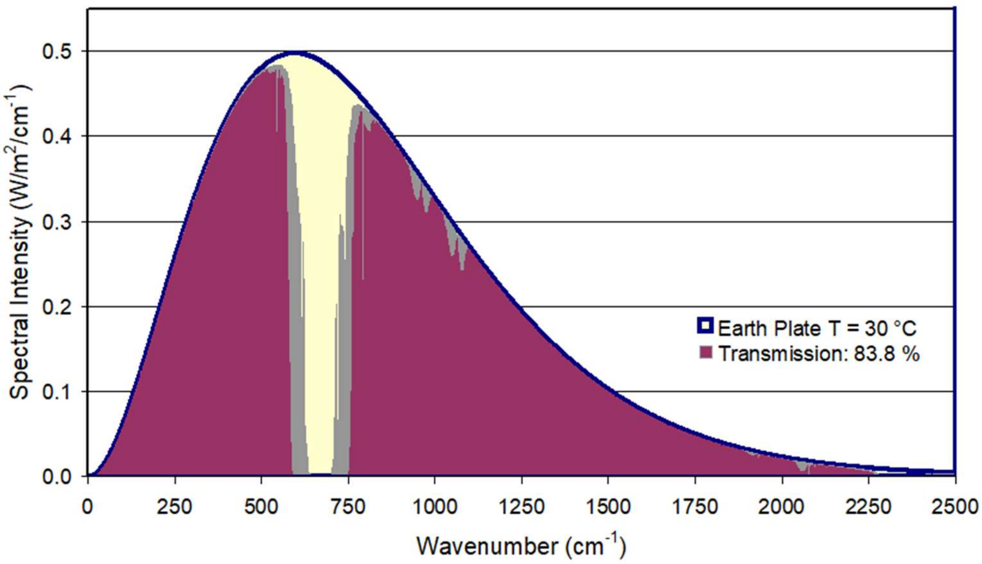


Figure 2: Spectral intensity radiated by the earth plate at T_E =30°C (Blue Graph) as a function of wavenumbers. Transmission of initial radiation through 20% CO_2 in dry air at a temperature of 20°C and over a pathlength of 111 cm is shown in Plum color.

For these calculations we use the program-platform MolExplorer (Harde & Pfuhl, 2012 [20]) with access to the HITRAN-database (Rothmann et al., 2009 [18]) and applying Lambert-Beer's law with an exponential decline of a spectral component $I_{\tilde{\nu}}(0)$ over a layer thickness z:

$$I_{\tilde{\nu}}(z) = I_{\tilde{\nu}}(0) \cdot e^{-2 \cdot \overline{\alpha}(\tilde{\nu}) \cdot z}, \qquad (2)$$

where $\overline{\alpha}(\tilde{\nu}) = \sum_i \overline{\alpha}^i_{nm}(\tilde{\nu})$ represents the effective spectral absorption coefficient, expressing the

difference between induced absorption and induced emission processes and summed over all lines i with transitions n $\rightarrow$ m at wavenumber $\tilde{\nu}$. We note that different to the spectral radiance $I_{\tilde{\nu},\Omega}(z)$ for the spectral intensity $I_{\tilde{\nu}}(z) = \int I_{\tilde{\nu},\Omega} d\Omega = \pi \cdot I_{\tilde{\nu},\Omega}$ as integral over all propagation directions within one hemisphere, the mean pathlength of radiation to cross a layer-thickness L in z-direction (perpendicular to the emitter surface) is twice this depth (see Harde [19], Subsec. 3.2). This is the case for atmospheric layers, and this also holds in good approximation for a set-up as used here, where the radiation suffers from multiple reflections at the walls, before it is absorbed at the cold plate.

Under these conditions the total absorption by the gas sample is 16.2%. In the atmosphere with a CO_2-concentration of 400 ppmv and neglecting interference with water vapor lines this corresponds to an atmospheric layer thickness of 555 m. But to make this clear, in both these cases the forgoing considerations and the graph in Fig. 2 only describe the fraction of incident radiation which is absorbed and released as heat in the gas, but it does not consider any eigen-radiation of the gas, which is superimposing the incident radiation and modifying the observed radiation and energy balance.

A complete and realistic simulation of measurements with a set-up as described in Section 2 requires to include this emission, which appears in the same spectral range as the earth plate radiation and which can significantly reduce the effective absorption losses, can modify the spectral distribution and is the origin of new up- or down-welling radiation. A first consideration of such Radiation Transfer (RT) - although dealing with radiation in the solar atmosphere - goes back to Schwarzschild (1906) [21].

3.2 Radiation Transfer

3.2.1 Thermal Emission of a Gas

Atoms and molecules are not only absorbing on their resonance transitions, they also emit on these transitions, well known as spontaneous emission. While the mean lifetime of an electronically excited state typically lies in the nanosecond regime before such an emission on a visible or ultraviolet transition to a lower lying state takes place, the lifetime of ro-vibronic states with transitions in the IR or far-IR range easily attains milliseconds to seconds. At regular atmospheric conditions then de-excitation due to collisions with buffer gases (N_2 and O_2 - superelastic collisions of 2nd type) at collision rates in the GHz-range is much more probable, and the absorbed energy of the incident radiation is no longer re-emitted but transferred into kinetic energy and released as heat in the gas. Fig. 2 was calculated for such conditions.

Indeed, can this behavior be observed and is quite successfully used for one of the most sensitive detection methods for trace gases in the atmosphere, the photo-acoustic effect (Wolff & Harde 2003 [22]; Harde et al. 2010 [23]): *The incident radiation resonantly interacting with the molecules, is modulated and the periodically generated heat is detected as acoustic wave by a microphone.* But often is such heat transfer misinterpreted in a way that any radiation of GH-gases in the troposphere, particularly back-radiation, is completely quenched. This is by far not the case.

Different to electronic states the lower lying ro-vibronic levels can also be populated by inelastic collisions (collisions of 1st type) with an excitation rate (from lower level n to upper level m):

$$C_{nm} = \frac{g_m}{g_n} e^{-\frac{h \cdot c \cdot \tilde{\nu}_{mn} \cdot 100}{k_B T_G}} C_{mn}, \qquad (3)$$

which is proportional to the transition rate C_{mn} due to superelastic collisions and proportional to the Boltzmann-distribution with T_G as the gas temperature, $\tilde{\nu}_{mn}$ as the transition wavenumber and g_i as statistical weights of the involved states (see also, Harde 2013 [19], eq. 36). This continuous re-population of an excited state by inelastic collisions also ensures radiative transitions, which occur independently from any collision induced transitions (see, Harde [19], Subsec. 2.5). This

spontaneous emission of molecules defines the thermal radiation of a gas. Because of its origin this radiation only exists on discrete frequencies, given by the transition frequencies and the linewidths of the transitions. But on these frequencies and over longer paths the radiation strength is the same as that of a blackbody radiator, and at thermal equilibrium it is only controlled by the gas temperature T_G.

Such thermal or background radiation in the atmosphere has been observed as upwelling radiation by satellites (Tobin 1986 [24]) and as downwelling radiation at ground-stations (Arnott 2008 [25]; Feldmann et al. 2015 [26]). This excludes any doubts on the existence of this radiation also under conditions as found in the lower troposphere (see also Harde 2013 [19], Figs 21 and 22).

3.2.2 Schwarzschild-Equation

As the emission on a spectral line is directly related to the absorption strength on this transition, the spontaneous or thermal emission of the gas can be shown to be proportional to the absorption coefficient $\overline{\alpha}_{nm}(\tilde{\nu})$ on this line and the Kirchhoff-Planck function $B_{\tilde{\nu}}(T_G(z))$, which is of the same type as (1b), but describes the spectral intensity of the gas at temperature T_G and position z. Over shorter distances *dz* then changes in the spectral intensity $I_{\tilde{\nu}}(z)$ of the incident radiation can be expressed as a modification of Lambert-Beer's law (in differential form) with an absorption and emission term:

$$\frac{dI_{\tilde{\nu}}(z)}{dz} = 2 \cdot \overline{\alpha}(\tilde{\nu}, z)\big(-I_{\tilde{\nu}}(z, T_E) + B_{\tilde{\nu}}(T_G(z))\big). \qquad (4)$$

This is the Schwarzschild-equation for the spectral intensity, derived under conditions of a local thermal equilibrium in the gas (cf. Harde [19], eq. (92)). It describes the radiation transfer in the gas in the presence of absorption and thermal emission. The factor 2 again accounts for the mean pathlength of radiation to cross the layer thickness *dz*.

In general, the density of the gas, the total pressure and the temperature are changing over the propagation path. Thus, (4) has to be solved stepwise for thin layers of thickness Δz, over which, $\overline{\alpha}(\tilde{\nu}, z)$ and $B_{\tilde{\nu}}(T_G(z))$ can be assumed to be constant (see Fig. 3).

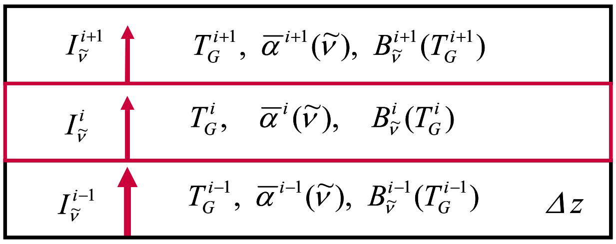


Figure 3: Stepwise calculation of the spectral intensity for the radiation transfer in a gas.

Integration of (4) for the *i*-th layer with initial conditions from layer *i*-1 then gives:

$$I_{\tilde{\nu}}^{i}(\Delta z) = I_{\tilde{\nu}}^{i-1} e^{-2\overline{\alpha}^{i}(\tilde{\nu})\Delta z} + B_{\tilde{\nu}}^{i}(T_G^{i}) \cdot (1 - e^{-2\overline{\alpha}^{i}(\tilde{\nu})\Delta z}). \qquad (5)$$

The first term in (5) describes the transmission of the incident spectral intensity over the layer thickness, while the second term represents the self-absorption of the thermal background radiation in forward direction and is given by the spontaneous emission of the layer into one hemisphere.

3.2.3 Some First Consequences

A special case of RT is given, when the gas has the same temperature as an internal or external blackbody radiator. Then, from (4) or (5) we directly see that the outgoing intensity is the same as the incident intensity. Changes can only be expected, when T_E and T_G are different and/or T_G varies over the pathlength.

This already explains, why it is difficult to verify the GHE when only looking to the gas temperature. Net absorption and thus heating of the gas by incident radiation only takes place as long as the respective spectral intensity on the molecular transitions is larger than the eigen-radiation of the gas on these lines. When this has equalized, no further net exchange happens, and in this sense RT in the gas acts similar to heat conduction and convection equalizing local temperature differences.

A larger local and global warming of a GH-gas is also restricted by its own radiation. This limits the effective absorption from an IR or visible light source and impedes distinction of this contribution from the dominating waste heat released by these sources. All this is further aggravated in the presence of heat conduction and convection in a typical set-up.

A prerequisite for the observation of the GHE in the atmosphere and in the same way in a laboratory experiment is a temperature gradient in the gas, otherwise no net changes in the radiation balance can be expected.

3.2.4 Forward-Radiation

Fig. 4 shows a Line-By-Line-Radiation-Transfer (LBL-RT) calculation for 20% CO_2 in air over 111 cm. But different to Fig. 2 varies the gas temperature over the propagation length from 30°C at the earth plate to −11.4°C at the cooled plate. This corresponds to a lapse-rate of 0.373°C/cm over the gas column. The emitted radiation of the earth plate is indicated as Blue Graph on a yellow background, the transmitted spectral intensity in front of the cold plate is displayed in Plum, and the weak absorption bands as well as the semitransparent wings are plotted in Grey. The significantly lower absorption with 5.2% compared to Fig. 2 with 16.2% is obvious and is the result of the eigen-emission of the gas.

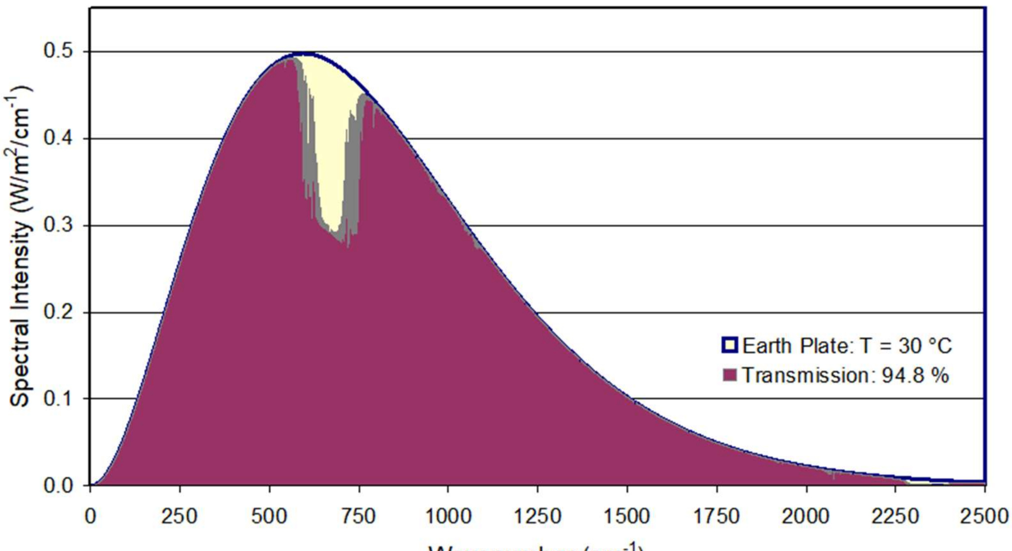


Figure 4: LBL-RT-calculation for 20% CO_2 in air over 111 cm for a lapse rate of 0.373°C/cm. Plotted is the blackbody radiation for 30°C (Blue-Yellow) and the transmitted spectral intensity (Plum-Gray).

This calculation is based on (5) and was performed with a layer thickness of Δz = 1 cm. For each layer the spectral changes of more than 12,000 lines with their pressure and temperature dependent linewidths have to be calculated to finally derive the transmitted intensity after 111 calculation steps. The pressure in the tank was assumed to be constant and the gas density considered to change according to the ideal gas equation.

Fig. 4 reproduces conditions as recorded by satellites (Tobin 1986 [24]) measuring the upwelling radiation or forward scattering, which is characterized by the typical funnel around 670 cm^{-1}. In

this spectral range is the incident radiation completely absorbed (see Fig. 2), and the observed intensity only results from thermal emission of the gas at reduced temperatures close to the lower plate. In this case the gas first absorbs 73.6 W/m^2 from the incident radiation of 479 W/m^2 (integral over the spectral intensity) and emits again 48.5 W/m^2, while a difference of 25.1 W/m^2 remains in the gas volume and can contribute to warming and/or radiation, as long as this is not lost at the walls.

To detect the forward or upwelling radiation is one way to verify the GHE, the other approach, we prefer in this contribution, is to measure the downwelling or backward radiation. In analogy to the terrestrial radiation we define the propagation from the warmer to the colder plate as positive z-direction and as upwelling radiation, although our set-up is just upside-down to EASy.

3.2.5 Back-Radiation

We have to remind that a full radiation balance has not only to consider the emission of the earth plate and the interaction with the gas but also the radiation emitted by the cold plate, which is propagating in anti z-direction through the gas towards the warmer plate. Thus, to simulate the RT for this case, we start with the spectral intensity emitted from the cold plate at $T_C = -11{,}4°C$ = 261.75 K and calculate the propagation through the gas cloud for a negative lapse rate c_T = –0.373°C/cm. Fig. 5 shows the spectral intensity of the back-radiation for 20% CO_2 in air over 111 cm (Plum-Gray).

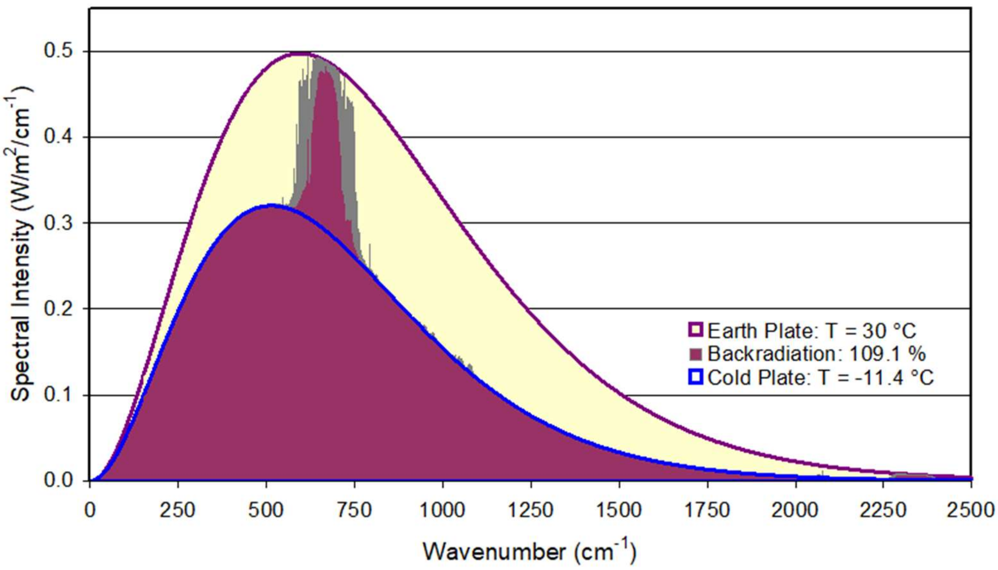


Figure 5: LBL-RT-calculation for 20% CO_2 in air over 111 cm for a lapse rate of -0.373°C/cm: Back-radiation from cold plate and gas (Plum-Gray), radiation only from cold plate (Blue) and spectral intensity of earth plate (Red-Yellow).

Also plotted is the emitted spectral intensity of the cold plate (Blue Line) and the earth plate (Red-Yellow). The eigen-radiation of the gas towards the warmer earth plate can well be identified as peak around 670 cm^{-1} (Plum area, Gray wings) on top of the broader spectrum of the lower plate. On the stronger lines at the band center the gas emission already attains saturation with spectral intensities, which are the same as those emitted by the earth plate in this spectral range.

Compared to the total radiated intensity of the cold plate with $I_C = \int I_{\tilde{\nu}} \cdot d\tilde{\nu} = 266\,\mathrm{W/m^2}$ the back-radiation increases by 24.2 W/m^2, which is 9.1%. This larger back-radiation is almost identical to the losses in forward direction, so that within observational accuracies the total balance of absorption and emission of the gas is zero. This is a further important aspect that speaks against measuring the gas temperature to prove the GHE. On the other hand, under the given conditions and with the apparatus presented in Section 2, it is quite possible and realistic to detect the radiation emitted

by the gas through a temperature rise of the earth plate.

4. Preliminary Studies and Calibration of the Measuring System

So far, our foregoing considerations were implicitly assuming a radiation transfer between sufficiently extended parallel plates without taking account of transversal or reflection losses in a laterally restricted radiation channel. For a direct comparison with a measurement therefore two preparatory investigations are required:

1. Assessment of radiation losses from one plate to the other.
2. Calibration of the earth plate's temperature response to the absorbed radiation.

4.1 Assessment of Radiation Losses

For the further characterization of the set-up it is advisable to distinguish between radiation losses without and with GH-gases in the radiation channel.

4.1.1 Without Infrared-Active Gases

According to our previous considerations, in the absence of GH-gases the total radiation from the lower half-plane, absorbed by the earth plate, results from the direct radiation of the cold plate. In general, however, this is additionally superimposed by radiation emitted by the side walls. Both these fractions suffer from geometrical and reflection losses on the way to the earth plate and have to be quantified in their relative and absolute contributions for a further analysis of the experiments. This is possible by measuring the electric heating power for the earth plate necessary to stabilize its temperature at 30°C while changing the temperature T_C of the cold plate over a wider range.

At thermal equilibrium the radiation and energy balance for the earth plate - or equivalently the balance of intensity fluxes - requires that all losses are just compensated by respective influxes.

Losses: As radiation losses of the earth plate only the emission to the lower half-space has to be considered, while any fluxes between the plate and dome with almost identical temperature are well balanced. The emitted intensity $I_E(T_E)$ of the earth plate at temperature T_E (in K) is the integral over Planck's distribution (1) and equivalent to the Stefan-Boltzmann-equation:

$$I_E(T_E) = \varepsilon_E \int I_\lambda(T_E) \cdot d\lambda = \varepsilon_E \int I_{\tilde{\nu}}(T_E) \cdot d\tilde{\nu} = \varepsilon_E \cdot \sigma_B \cdot T_E^4, \qquad (6)$$

with $\varepsilon_E \approx 1$ as the emissivity of the black colored plate and $\sigma_B = 5.67 \cdot 10^{-8}$ W/m^2/K as the Stefan-Boltzmann constant.

An additional loss has to be included, which is determined by heat conduction of the gas, mostly from the warmer plate to the walls. It is designated as $L(\Delta T)$ for a temperature gradient ΔT.

Savings: Radiation influxes come from the cold plate and the walls. The cold plate with an emitted intensity $I_C(T_C)$ at temperature T_C then contributes the fraction f_C to the energy balance, and the walls with a radiated intensity $I_W(T_W)$ at temperature T_W the fraction f_W. Additionally we include radiation of the earth plate itself, which is partially back-reflected from the walls with the amount $R_E(I_E)$. While the intensities can be calculated for the respective temperatures from (6), the fractions f_C and f_W and also the reflection R_E, which are representing all geometrical as well as reflection and re-emission losses on the way to the earth plate are for now unknown.

All fluxes, positive and negative ones, determine together the theoretical heating intensity H_E (electric heating power per cross section) required to stabilize the earth plate on the temperature T_E:

$$H_E^T(T_C, T_W) = I_E(T_E) - f_C \cdot I_C(T_C) - f_W \cdot I_W(T_W) - R_E(I_E) + L(\Delta T). \qquad (7)$$

This balance is used to calculate the necessary plate heating and to compare it with the measured heating, when the temperature of the cold plate and thus, the intensity I_C is changed while leaving all other parameters - as far as possible - the same (as an example see: Appendix 4, Table A4.1).

In Fig. 6 is plotted the measured heating H_E as a function of the intensity $I_C(T_C)$ (Magenta Diamonds) when changing the temperature from –12.6°C up to +10.5°C (260.6 - 283.6 K). The data show a straight line reflecting that any changes mostly can be traced back to intensity variations of the cold plate and obey Stefan-Boltzmann's equation. Heat conduction in the gas, varying linearly on a temperature scale, would cause larger deviations on the intensity scale, and thus, can widely be excluded. Also radiation changes from the walls, inclusive radiation from the earth plate, that is back-reflected from the walls, can be neglected, since primarily radiation from the upper section of the tank hits the earth plate, where the wall is only very little affected by temperature variations of the cold plate. All measurements were repeated 10 times and show excellent reproducibility.

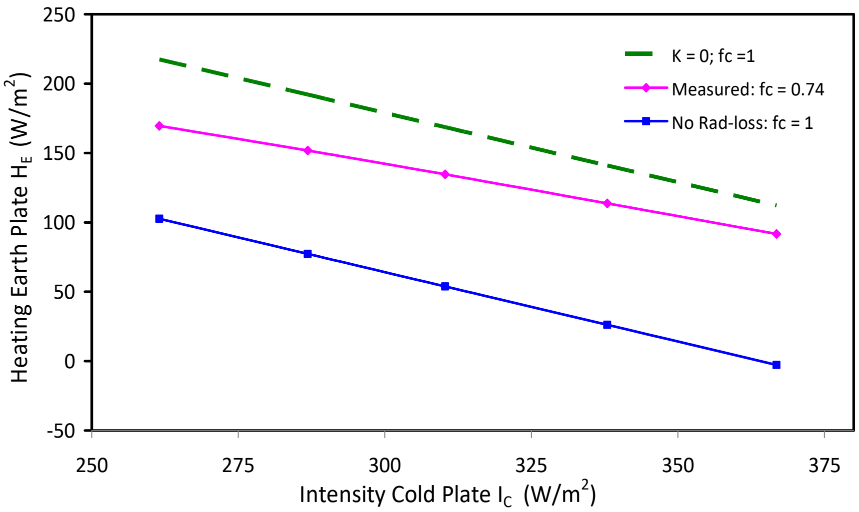


Figure 6: Measured heating of earth plate for a fixed temperature T_E of 30°C as a function of the radiated intensity I_C of the cold plate (Magenta Diamonds). Also plotted is the expected heating for f_C = 1 (Blue Squares) and $K(T_W,\Delta T)$ = 0 (Green Dashed).

Often deniers of the GHE argue that radiation from a cooler body cannot be absorbed by a warmer body, as this would be a violation of the 2nd law of thermodynamics. This relatively simple measurement is clear evidence of a wrong interpretation of this law, which explicitly includes the "*simultaneous double heat exchange by radiation"* (Clausius). In a closed system "*the colder body experiences an increase in warmth at the expense of the warmer body",* which on its own experiences a lower cooling rate. In an open system with external heating this even leads to an increasing temperature of the warmer body in the presence of additional back-radiation from a colder body.

According to (7) is the slope of the measured heating H_E the fraction of the transmitted radiation from the cold to the warm plate, for which we derive a value f_C = 0.74, i.e., 74% of the theoretically expected emission of the cold plate arrives at the earth plate. For comparison is also plotted the case of zero radiation losses, when $\Delta H_E = \Delta I_E$ (f_C= 1) (Blue Squares).

For the limiting case T_C = 0 K, thus $I_C(0)$ = 0, extrapolation of the measured data gives $H_E(0,T_W)$ = 364.1 W/m^2. Then for the radiation flux from the walls (inclusive reflections of the earth plate emission) minus the heat conduction, together represented by the quantity K, we find with (7):

$$\begin{aligned} K(T_W,\Delta T) &= f_W \cdot I_W(T_W) + R_E(I_E) - L(\Delta T) \\ &= I_E(T_E) - H_E(0,T_W) = 478.9 - 364.1 = 114.8 \ \text{W/m}^2 \end{aligned}, \quad (8)$$

which can largely be regarded as constant over the measured temperature interval of 24°C (see also Appendix 3 and Appendix 4, Table A4.2).

According to Stefan-Boltzmann's law with a wall temperature of about 28°C in the upper section of the tank, an emissivity of the polished wall surface of $\varepsilon_W \approx 0.1$ and a relatively large assumed fraction $f_W \approx 0.85$ of the emitted wall intensity, the radiation from the walls does not contribute more than 40 W/m^2. That means, a relatively large fraction of at least 75 W/m^2 or 15.6% of the earth plate radiation must be back-reflected from the walls. So, for the heat conduction $L(\Delta T_E)$ acting with opposite sign there is not too much left in the energy balance, which shows its only moderate impact on the further investigations (see also Sec. 5). Note, the highest sensitivity for detecting changes of the cold plate and also radiation of a GH-gas is given when $K(T_W,\Delta T) = 0$ and $f_C = 1$. This is represented by the Green Dashed line in Fig. 6 as a quality reference for the set-up.

4.1.2 With Infrared-Active Gases

The previous investigations with dry air in the tank, while changing the temperature of the cold plate, give a first orientation, which radiation losses from the cold to the warm plate have to be expected. But they are also an important prerequisite for a measurement with a GH-gas in the housing to answer the question, what fraction of the gas radiation can be collected by the earth plate.

With a GH-gas in the radiation channel the energy and radiation balance has to be expanded by an additional term for the emitted intensity of the gas $\Delta I_G(T_C, c_T)$, which is changing with the temperature difference between the plates and thus with the lapse-rate c_T, and which contributes the fraction f_G to the total balance:

$$H_E^T(T_C, T_W, c_T) = I_E(T_E) - f_C \cdot I_C(T_C) - f_G \cdot \Delta I_G(T_C, c_T) - K(T_W, \Delta T)\,. \qquad (9)$$

We consider here the intensity $\Delta I_G(T_C, c_T)$, which is emitted on top of the radiation from the cold plate (see Fig. 5), since otherwise the spectral interval under the Planck curve would be counted twice. For the fraction f_G we assume that it does not change with the lapse rate and gas density. K summarizes again the wall radiation, reflection and heat conduction losses according to (8).

We have performed measurements for the three IR-active gases CO_2, CH_4 and N_2O, each with 10% concentration in dry air, and as further control runs additional measurements with 10% He and 20% Ar (Appendix 4, Table A4.3). The measuring procedure is the same as described in Subsec. 4.1.1), only exchanging the gas in the tank. As example we look closer to the measurements with the CO_2-mixture as sample gas.

Table 1: Measured heating of the earth plate at varying cold plate temperature with 10% CO_2 in air.

ΔT (°C)	$H_E(CO_2)$ W/m^2	H_E (air) W/m^2	ΔH_E W/m^2	c_T °C/cm	calc. ΔI_{CO2} W/m^2	$f_{CO2} = \Delta H_E/\Delta I_{CO2}$	$f_{CO2} \cdot \Delta I_{CO2}$ W/m^2
19.6	85.03	92.1	7.09	0.177	10.65	0.67	6.93
24.7	102.75	111.3	8.56	0.223	13.08	0.65	8.52
31.4	124.70	134.8	10.10	0.283	16.10	0.63	10.48
36.5	139.90	151.4	11.51	0.329	18.28	0.63	11.90
42.9	157.00	171.2	14.17	0.387	20.86	0.68	13.58
					mean f_{CO2}:	0.65	

Table 1 displays the recorded heating in units of W/m^2 (column 2) as a function of the temperature difference ΔT between the earth plate (fixed temperature at 30°C) and the varying temperature of the cold plate (column 1). Also listed is the measurement in dry air from Subsec. 4.1.1), which works as reference for the further evaluation (column 3).

The difference between the air- and CO_2-measurements ΔH_E, displayed in column 4, then can be

compared with calculations as presented in Section 3. The RT-calculations for ΔI_{CO2} caused by 10% CO_2 and for a laterally extended plane of L = 111 cm depth (the average propagation path is $2 \cdot L = L/\cos\beta$ with $\beta = 60°$ as mean propagation angle) is a function of the lower plate temperature T_C or the lapse-rate (column 5) and listed in column 6.

ΔI_{CO2} is plotted in Fig. 7 (Magenta Diamonds) as a function of the temperature differences ΔT between the plates and can directly be compared with the measured differences ΔH_E (Blue Squares). The ratio of the measured to calculated difference defines the fraction $f_{CO2}=\Delta H_E/\Delta I_{CO2}$ of emitted CO_2 radiation, which contributes to the heating of the earth plate. As average over the different temperatures we find f_{CO2} = 0.65, which gives a further orientation for the expected contribution of CO_2 to the radiation balance. The trend curve as mean $f_{CO2} \cdot \Delta I_{CO2}$ is shown as Green Triangles.

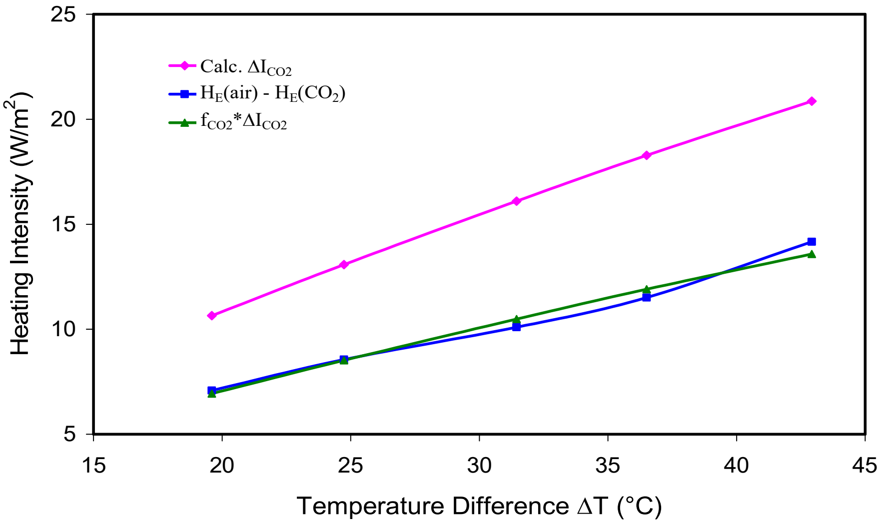


Figure 7: Calculated back-radiation ΔI_{CO2} (Magenta Diamonds), measured difference ΔH_E (Blue Squares) and theoretically expected heating $f_{CO2} \cdot \Delta I_{CO2}$ at 10% CO_2 in air (Green Triangles).

Based on the same procedure we derive the respective fraction for 10% CH_4 in dry air with f_{CH4} = 0.64 and for 10% N_2O in air with f_{N2O} = 0.62. Within our observational limits there exist no larger specific deviations between these gases, which coincide within an accuracy of less than 5%.

The relatively smaller fractions for the gas emission compared to the cold plate have to be explained by the fact that for the gases only the difference on top of the plate emission and not their full emission is considered (Fig. 5). Further differences result from a volume radiator to a surface emitter and the geometry.

A smaller change in the energy balance might also be expected due to differences in the heat conduction of the GH-gas relative to air. Therefore, control measurements with the noble gases He and Ar were performed, He with a significantly higher conductivity, Ar with a lower conductivity than air and comparable with CO_2 and N_2O. But within our measuring accuracy no differences between the noble gases and air in the energy balance can be observed (see Appendix 3). Thus, based on these experiments heat conduction as a reason for the observed changes can well be excluded.

4.2 Temperature Calibration of Earth Plate

In the previous subsection we looked to the correlation between the electric heating $H_E(T_C)$ required to stabilize the temperature of the earth plate at 30°C, when the radiated intensity $I_C(T_C)$ of the cold plate is changed. Now the temperature of the cold plate is held fixed at -11.4°C and the temperature T_E of the earth plate measured as a function of the plate heating $H_E(T_E)$. This

correlation describes the temperature sensitivity λ of the apparatus, i.e., the increase of the plate temperature ΔT_E when the heating H_E is increased by 1 W/m^2:

$$\Delta T_E = \lambda \cdot \Delta H_E(T_E)\,. \qquad (10)$$

Also for the characterization of EASy, almost all known models are based on such simple relation that the ground temperature changes are scaling proportional with the changes of an external forcing ΔF. In its 6th Assessment Report (AR6) [27] the Intergovernmental Panel on Climate Change (IPCC) assumes that this forcing is almost exclusively caused by anthropogenic emissions of CO_2 with an expected likely temperature increase (including feedback effects) of 2.5 - 4°C for a doubling of the CO_2 concentration. The proportionality factor for characterizing EASy is called the Planck sensitivity λ_P or climate sensitivity parameter with $\lambda_P \approx 0.31$°C/W·m^2 (AR6-WG1-Sec.7.4).

In this context we note that different to the general understanding of radiative forcing as the net difference of radiative fluxes at the tropopause or at the top of the atmosphere, here we consider directly the measured and calculated down-welling flux ΔF at the earth plate. But RT-calculations show that their absolute contributions are almost identical (see: Subsec. 3.2.4 and 3.2.5).

In our case is λ a process parameter of the set-up that reflects the radiation exchange and heat losses. But dependent on the process-related heat losses, λ can be found to change considerably.

A measurement according to (10) starts at an initial temperature of the earth plate of T_E = 25°C and is recorded as a function of the stepwise increased heating intensity H_E. This can be performed

- with a constant dome temperature of 30°C, as applied in the previous subsection or
- with an adapted dome temperature $T_D = T_E$ to avoid a temperature difference to the earth plate.

Fig. 8 shows the difference of the two variants on λ, which gives λ = 0.082 °C/(W/m^2) for a constant dome temperature and λ = 0.184 °C/(W/m^2) with a sliding temperature.

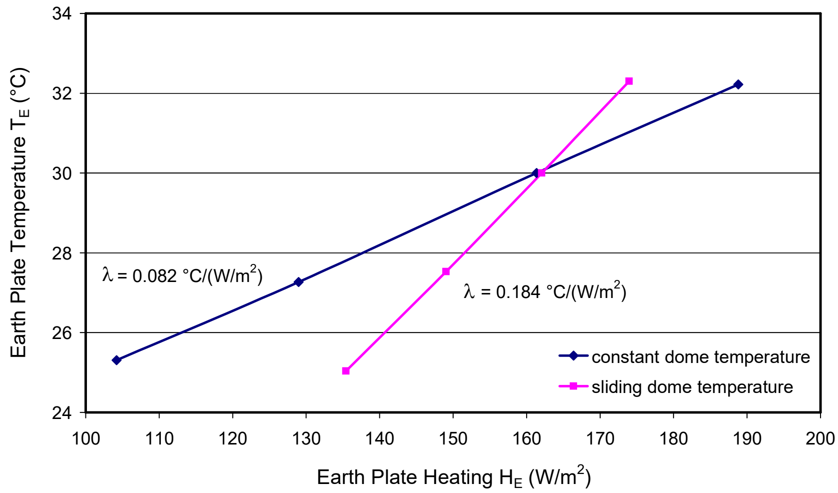


Figure 8: Temperature sensitivity for constant (Blue Diamonds) and sliding dome temperature (Magenta Squares).

The reason for this discrepancy is the different heat flow around the earth plate, which depends on the dome temperature. At constant T_D an incline of the plate temperature is strongly dampened by the increasing heat flow from the plate to the dome. At a sliding dome temperature, the loss is much lower and found as a steeper increase of the earth plate temperature with 0.184/0.082 = 2.24.

For our further investigations when directly measuring the warming of the earth plate as response to the back-radiation of GH-gases only the temperature sensitivity λ = 0.082 °C/(W/m^2) is of

relevance for comparison with theory, as all measurements are performed at a constant dome temperature.

5. Measurements and Calculation

In all experiments the temperature of the cold plate is -11.4°C and is not changed during an experiment. In a preparatory phase, the electric heating H_E of the earth plate is adjusted over the first 6 - 8 hours, till the temperature of the earth plate is exactly 30.0°C. Before adding a GH-gas to the chamber, all components of the setup must come to thermal equilibrium, as controlled by the temperature measurements taken during the first 60 minutes before the sample gas is added. The accuracy of the temperature reading is ± 0.13°C, which can only further be increased by independent measurements and averaging over several runs.

After filling the tank with a GH-gas the actual measurement is started by recording the temperature of the earth plate, and as further control, also temperatures at different positions over the gas column and at the cold plate. This happens without any external intervention till again equilibrium and a constant temperature increase ΔT_E of the earth plate is found. Then the electric heating is reduced to return to 30°C at the earth plate, allowing a direct measurement of the back radiation as difference of the required electrical heating ΔH_E of the earth plate (Fig. 9). The measurement process is explained in detail in Appendix 1.

From our investigations in Subsection 4.1b) and Appendix 3 we know that changes in the heat conductivity are negligible and the changes in H_E should directly represent the gas radiation $f_G \cdot \Delta I_G(T_C,c_T)$ collected by the plate.

5.1 CO_2-Measurement

Fig. 9 displays a typical plot, in this case for 10% CO_2 over the full recording time. The different graphs indicate the measured temperatures from the earth plate (Red), the dome (Green) and the gas at different positions over the radiation channel (T_1 - T_4, see Fig. 1).

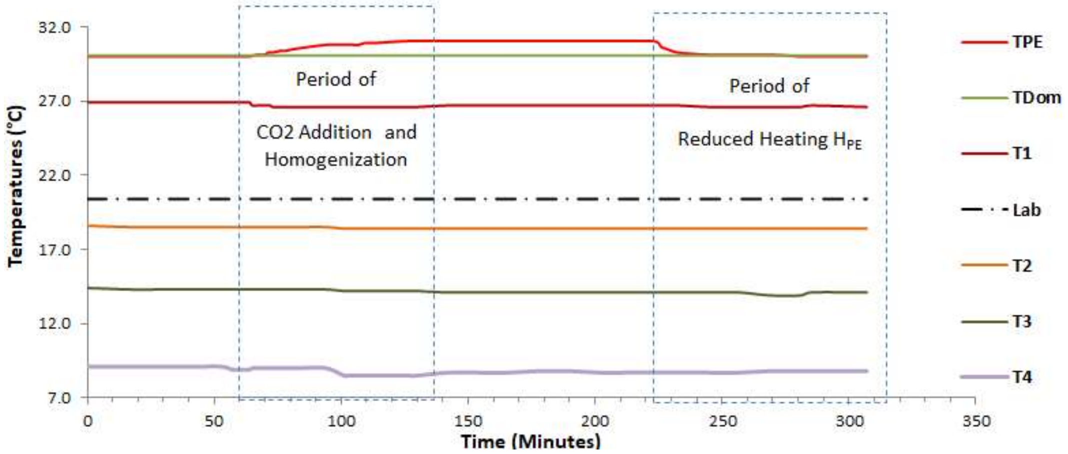


Figure 9: Typical measurement cycle, here for 10% CO_2 in dry air. Plotted are the temperatures of the earth plate (Red), the dome (Green), the gas temperature at 4 positions (T_1 - T_4) and the laboratory temperature (Black).

During the filling and recycling period of the gas smaller temperature deviations over the tank height can be observed, but when stopping this recycling, all temperatures except T_E return to their initial position. After 220 minutes the electric plate heating is reduced, till the earth plate temperature again attains 30°C.

To quantify the back-radiation of CO_2 with increasing concentration, and thus, to determine its impact on global warming, we have performed measurements over a wider range from 1.25% up

to 20% in dry air. From one measurement to the next each time the concentration is doubled up to 16x. All measurements represent the average of 5 independent runs. The results are displayed in Table 2.

Table 2: Measured earth plate temperature change ΔT_E and plate heating change ΔH_E as a function of the CO_2 concentration and comparison with RT-calculations.

CO_2	Earth Plate (°C)	Cold Plate (°C)	λ_{av} (°C/W·m²)	c_T (°C/cm)	f_{CO2}	log start ΔT_0(°C)	ΔF_{2xCO2} (W/m²)
	30.0	-11.4	0.083	-0.373	0.59	0.45	3.70
Con-cen (%)	Meas. ΔT_E (°C)	Meas. ΔH_E (W/m²)	$\lambda=\Delta T_E/\Delta H_E$ (°C/W·m²)	Calc. ΔI_{CO2} (W/m²)	$f_{CO2} = \Delta H_E/\Delta I_{CO2}$	$\lambda_{av} \cdot f_{CO2} \cdot \Delta I_{CO2}$ (°C)	log fit ΔT_E (°C)
1.25	0.45	5.05	0.089	9.92	0.51	0.49	0.45
2.5	0.63	7.44	0.085	13.05	0.57	0.64	0.63
5.0	0.79	9.76	0.081	16.48	0.59	0.81	0.81
10.0	1.00	11.80	0.085	20.15	0.59	0.99	0.99
20.0	1.18	14.09	0.084	24.13	0.58	1.18	1.17

Column 2 shows the measured temperature increase ΔT_E and column 3 the reduced plate heating ΔH_E. Their ratio (column 4) allows to determine independently the temperature sensitivity λ, which as average of these measurements is found to be a few % larger than in Subsec. 4.2. Therefore, as a basis for the further evaluation of the data we use a mean sensitivity $\lambda_{av} = 0.083$ °C/(W/m²). Column 5 specifies the calculated back-radiation ΔI_{CO2}, and column 6 the ratio of $\Delta H_E/\Delta I_{CO2}$. This ratio directly gives the fraction f_{CO2}, which contributes to the heating of the earth plate. The average deviates by 12% from the previously derived value of 0.65 in Subsec. 4.1.2, which was found by varying the cold plate temperature T_C up to 24°C. Since these measurements allow direct deduction of f_{CO2} with only little or no temperature changes in the system and including smaller absorption losses from the wall radiation, we use for the further evaluation a mean value of $f_{CO2} = 0.59$. The calculated temperature change $\Delta T_E = \lambda_{av} \cdot f_{CO2} \cdot \Delta I_{CO2}$ as a function of the CO_2-concentration is listed in column 7. The last column displays a logarithmic fit (log-fit) to the measurements.

Plotted in Fig.10a) is the measured temperature increase ΔT_E as a function of the CO_2-concentration (Blue Diamonds, col. 2) and as direct comparison the calculation $\lambda_{av} \cdot f_{CO2} \cdot \Delta I_{CO2}$ (Magenta Squares, column 7). Additionally displayed is the calculated CO_2 radiation ΔI_{CO2} (Green Diamonds, column 5).

Despite the short propagation path all graphs show clear saturation with increasing CO_2 concentration, and in the same way also the emission saturates at these concentrations. The temperature variation ΔT_E can well be represented by a logarithmic curve of the form:

$$\Delta T_E(C_{CO2}) = \Delta T_0 + \lambda_{av} \cdot f_{CO2} \cdot \Delta F_{2xCO2} \cdot \ln(C_{CO2} / C_0) / \ln 2 , \quad (11)$$

with ΔT_0 as the temperature increase at the concentration C_0, here 1.25%, and ΔF_{2xCO2} as radiative forcing when doubling the CO_2 concentration. Superimposed in Fig. 10a) is a fit based on (11) with $\Delta T_0 = 0.45$°C and $\Delta F_{2xCO2} = 3.70 \pm 0.05$ W/m² (Brown Crosses, column 8), which on first glance shows excellent agreement with Myhre et al. [28], but is derived under different conditions (see Sec. 6).

The measured plate heating variation ΔH_E as an independent means for detecting the back-radiation is plotted in Fig. 10b) (Blue Diamonds, column 3). It can directly be compared with the calculated back-radiation $f_{CO2} \cdot \Delta I_{CO2}$ (Green Triangles) with f_{CO2} as the free parameter for a fit to the measurements. From this fit we derive the fraction $f_{CO2} = 0.59$ of the emitted gas, which within our limits of observation is in good agreement with Table 2, column 6.

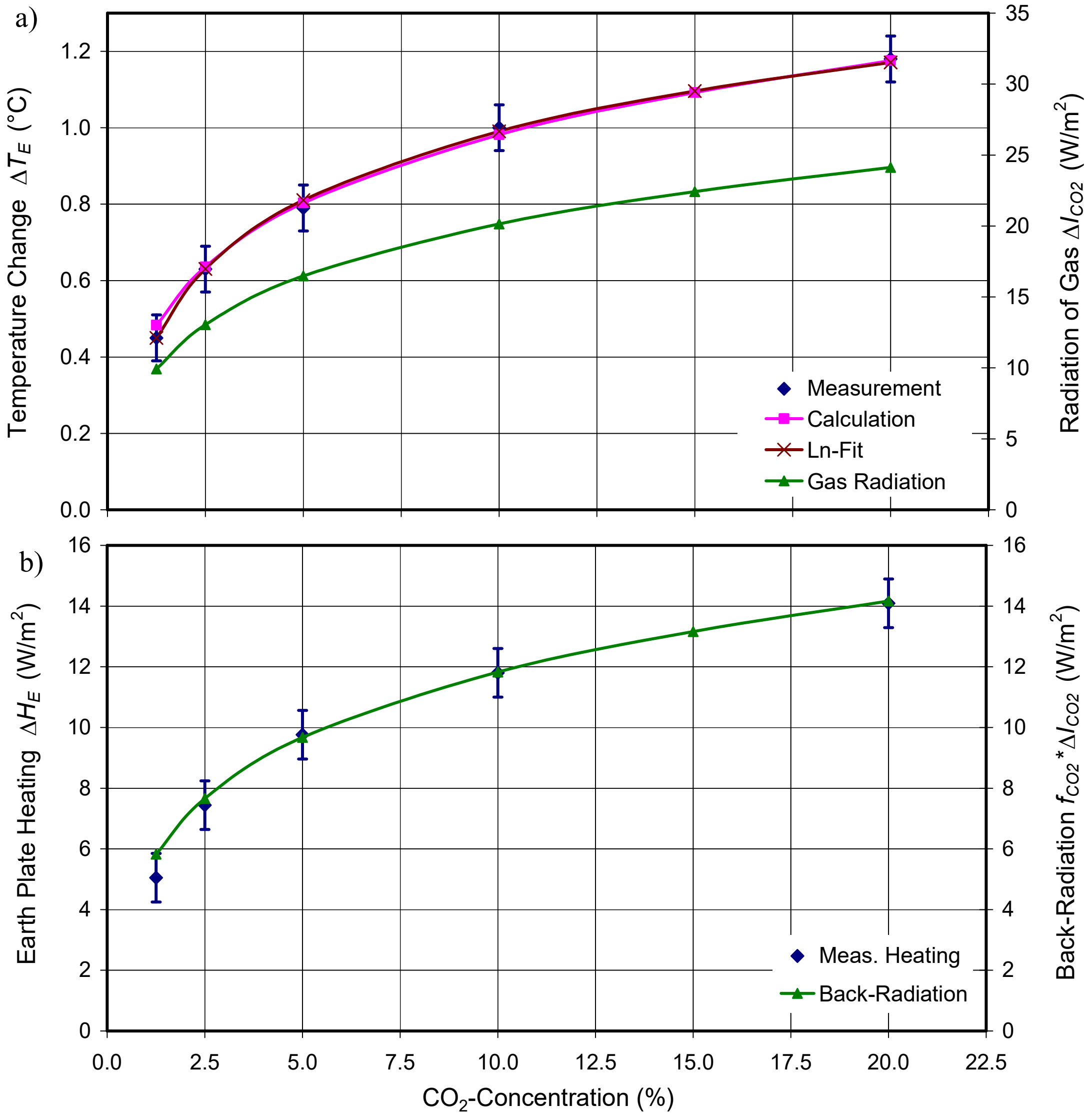


Figure 10: a) Measured temperature change of the earth plate as a function of the CO_2-concentration in dry air (Blue Diamonds) and calculation (Magenta Squares). Superimposed is a logarithmic fit (Brown Crosses) and the LBL-RT-calculation of the back-radiation ΔI_{CO2}. b) Comparison of measured plate heating ΔH_E (Blue Diamonds) and calculated back-radiation collected by the earth plate $f_{CO2} \cdot \Delta I_{CO2}$ for $f_{CO2} = 0.59$ (Green).

5.2 CH_4-Measurements

Measurements with CH_4 as sample gas were performed under identical experimental conditions as in Subsec. 5.1. The concentration was varied from 1.25% to 10%. Plotted in Fig. 11a) is the measured temperature variation ΔT_E of the earth plate with increasing CH_4-concentration (Blue Diamonds), which can directly be compared with the calculated temperature change $\lambda_{av} \cdot f_{CH4} \cdot \Delta I_{CH4}$ (Magenta Squares). The respective calculated CH_4 radiation ΔI_{CH4} is shown as Green Triangles.

The temperature sensitivity is the same as found previously (Subsec. 5.1) with $\lambda_{av} = 0.083$ °C/(W/m^2), and the fraction of CH_4 radiation, which contributes to the plate heating, is, independent from Subsec. 4.1, now confirmed by Fig. 11b) with $f_{CH4} = 0.64$ when comparing the measured plate heating ΔH_E (Blue Diamonds) with the calculated back-radiation $f_{CH4} \cdot \Delta I_{CH4}$ (Green Triangles).

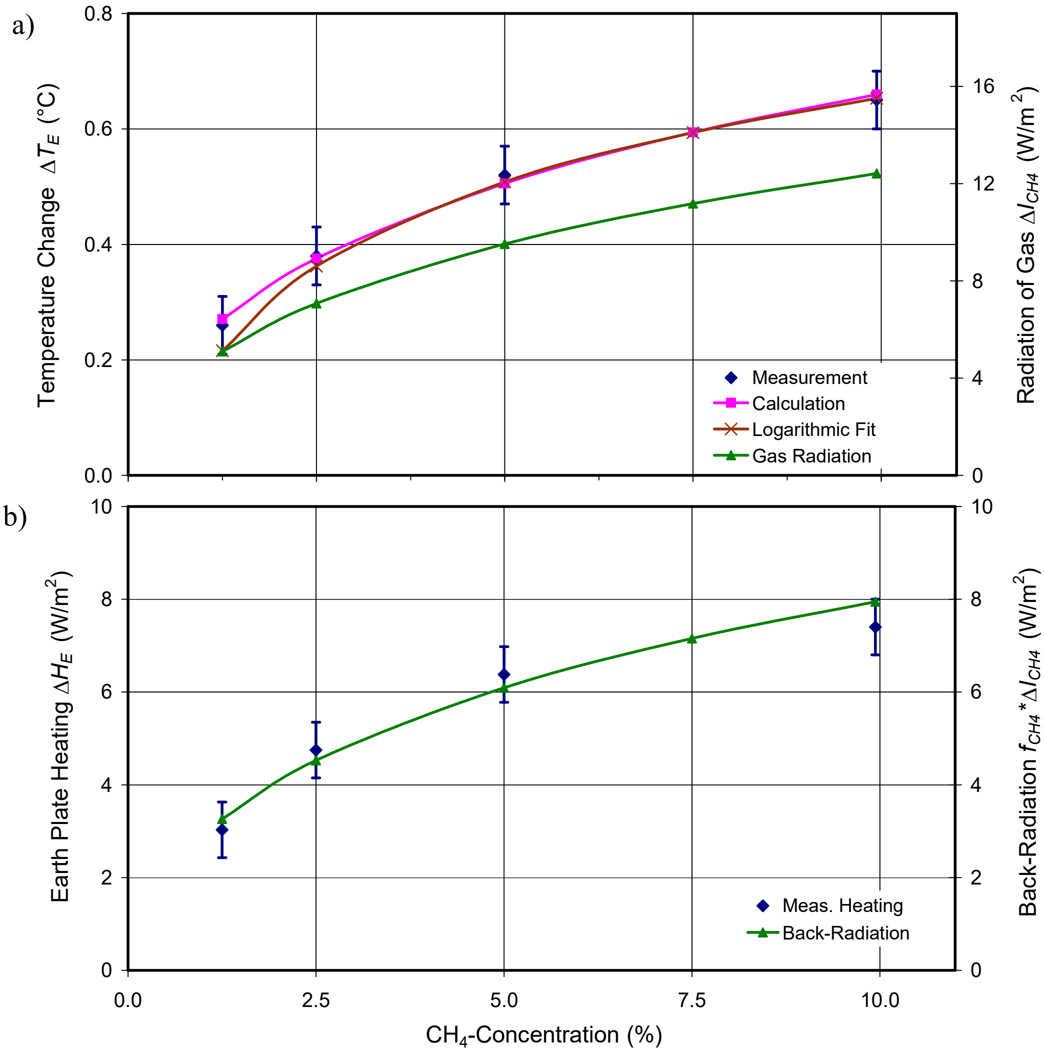


Figure 11: a) Measured temperature change of the earth plate as a function of the CH_4-concentration in dry air (Blue Diamonds) and calculation (Magenta Squares). Superimposed is a fit assuming a logarithmic function (Brown Crosses) and the LBL-RT-calculation of the back-radiation ΔI_{CH4}. b) Comparison of measured plate heating ΔH_E (Blue Diamonds) and calculated back-radiation collected by the earth plate $f_{CH4} \cdot \Delta I_{CH4}$ for f_{CH4} = 0.64 (Green Triangles).

As good approximation, except at the lower concentrations before the CH_4 lines come to saturation, can the measurement and the calculation again be represented by a logarithmic function:

$$\Delta T_E(C_{CH4}) = \Delta T_0 + \lambda_{av} \cdot f_{CH4} \cdot \Delta F_{2xCH4} \cdot \ln(C_{CH4}/C_0)/\ln 2\,, \qquad (12)$$

with ΔT_0 = 0.22°C at C_0 = 1.25% and ΔF_{2xCH4} = 2.75 W/m^2. A third-root approximation even shows still better agreement with the measurements and calculation, but to compare the forcing with the other gases and for the same concentration range, particularly at doubled concentration, we prefer a logarithmic representation.

5.3 N_2O-Measurements

The experimental conditions for the measurements with N_2O are the same as in Subsec. 5.1 and 5.2. The concentration was varied from 1.25% to 15%. Fig. 12a) displays the measured temperature variation ΔT_E of the earth plate with increasing N_2O-concentration (Blue Diamonds) and can again be compared with the calculated temperature change $\lambda_{av} \cdot f_{N2O} \cdot \Delta I_{N2O}$ (Magenta Squares). The respective theoretical N_2O radiation ΔI_{N2O} is shown as Green Triangles.

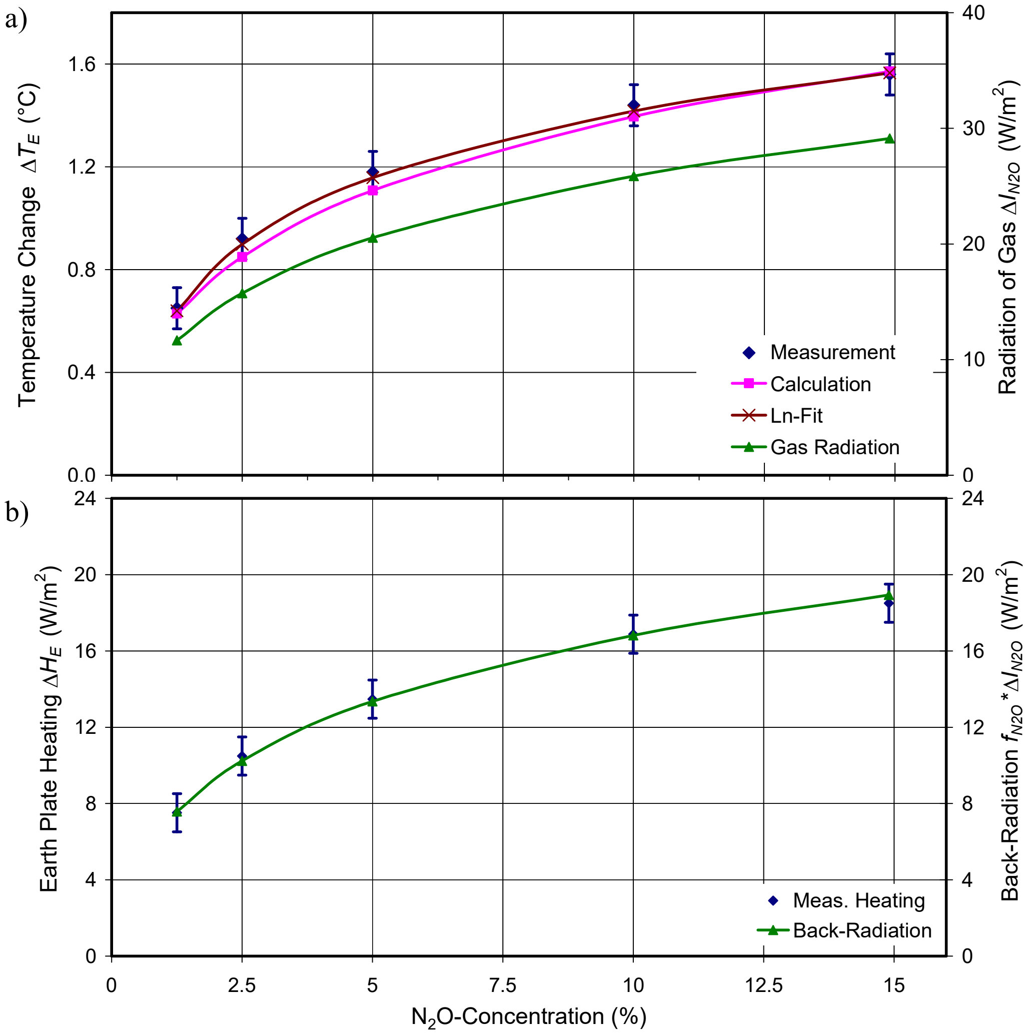


Figure 12: a) Measured temperature change of the earth plate as a function of the N_2O-concentration in dry air (Blue Diamonds) and calculation (Magenta Squares). Superimposed is a fit with a logarithmic function (Brown Crosses) and the LBL-RT-calculation of the back-radiation ΔI_{N2O}.
b) Comparison of measured plate heating ΔH_E (Blue Diamonds) and calculated back-radiation collected by the earth plate $f_{N2O}{\cdot}\Delta I_{N2O}$ for f_{N2O} = 0.65 (Green Triangles).

In Fig. 12b) is plotted the measured plate heating ΔH_E (Blue Diamonds) and the calculated back-radiation $f_{N2O}{\cdot}\Delta I_{N2O}$ (Green Triangles). From a fit of the theoretical back-radiation to the measurement we derive for the N_2O radiation contributing to the plate heating, the fraction f_{N2O} = 0.65, which agrees with the value deduced in Subsec. 4.1 within 5%. The temperature sensitivity is further assumed with $\lambda_{av} = 0.083$ °C/(W/m^2).

The measured temperature (see Fig. 12a), Blue Diamonds) can well be represented by a logarithmic curve (Brown Crosses) of the same type as (11) and (12) with:

$$\Delta T_E(C_{N2O}) = \Delta T_0 + \lambda_{av} \cdot f_{N2O} \cdot \Delta F_{2xN2O} \cdot \ln(C_{N2O}/C_0)/\ln 2\,, \qquad (13)$$

now with ΔT_0 = 0.62°C at C_0 = 1.5% and ΔF_{2xN2O} = 5.0 W/m^2. The agreement with the theoretical curve (Magenta) is not perfect but is still within our limits of observation. A better agreement with the calculated data but a slightly worse fit to the measurements can be obtained with:

$$\Delta T_E(C_{N2O}) = \Delta T_0 + \lambda_{av} \cdot f_{N2O} \cdot \Delta F_{2xCo} \cdot \sqrt[2]{(C_{N2O} - C_0)/C_0}\,, \qquad (14)$$

with ΔT_0 = 0.6°C, C_0 = 1.5% and ΔF_{2xCo} = 5.5 W/m^2, where ΔF_{2xCo} now only represents the forcing

at doubled concentration C_0. We note that such approximations different to a logarithmic function are well known in the literature (see, Myhre et al. [28]).

6. Discussion of Results

Differences to Atmospheric Conditions: The experimental set-up as presented in Section 2 has proven to be appropriate for demonstrating the atmospheric GHE in the laboratory. Although the pathlength through the atmosphere is about a factor of 80,000 larger than in the tank, this is partially compensated by a 500x higher concentration for CO_2, a 50,000x larger CH_4-concentration, and it is even significantly overcompensated for N_2O with an almost 500,000x higher concentration relative to the sea-level values. Not so much the absolute values are relevant, more important is the optical depth, which scales with the absorption coefficient × pathlength.

On the other hand is the lapse rate over the troposphere with 6.5°C/km 5.700x smaller than in our experiment, while the absolute temperature difference is almost comparable.

But most important for the verification of the GHE and the back-radiation from IR-active gases is their emission in the presence of collisions, and this under conditions as found in the lower troposphere. The experiments definitely confirm that GH-gases are radiating on their transitions, and within an optically thick layer even comparable to a black-body radiator at the same temperature as the gas.

Impact of Background Radiation: Under real atmospheric conditions is the back-radiation of the GH-gases superimposed by the much broader radiation from clouds, which in first approximation can be assumed as grey emitters at temperature T_{cl} and with a spectral distribution according to (1), only with an emissivity $\varepsilon < 1$. This can further be covered by Mie-scattering from aerosols or mist, and together they significantly enhance the observed GHE.

In our experiment clouds and any backscattering are represented by the cold plate and walls with their transmitted intensities, which additionally to the GH-gas emission are absorbed by the earth plate. This total back-radiation is strongly changing with the temperature of the cold plate T_C (see Subsec. 4.1a) and in this way simulates the impact of clouds of different heights, and thus temperatures. But it also affects the size of the GH-gas contribution, which depends on the temperature difference between the plates and by this on the lapse-rate. This contribution develops just opposite to the plate's fraction as demonstrated by the measurements in Subsec. 4.1b). Fig. 7 show the increasing absorption ΔH_E of the earth plate with rising temperature difference ΔT and vice versa. Transferred to the atmosphere this means that with clouds the back-radiation is larger than for clear sky, but the relative contribution caused by GH-gases is declining (Harde 2017 [29], Sec. 3 and 4.2).

Reproducibility and Accuracy: The reproducibility of the measurements is strongly dependent on the equilibrium conditions of the whole equipment before filling the compartment with the GH-gas, and this applies also for the further recording of data. The temperature reading is limited to ±0.13°C, and thus, essentially determines the accuracy of the measurements. Also, the electric plate heating is affected by the temperature reading, as any initial and final tracing to derive the difference ΔH_E, requires two temperature measurements. Apparently, this is the main reason for some deviations from one run to the next. Additional perturbations go back to slight variations of the room temperature, which can only be controlled within ±0.2°C.

The error for an individual measurement of the temperature increase ΔT_E and the reduced plate heating ΔH_E we estimate at the lower concentrations as ±20% and at the higher concentrations as about ±10%. However, the overall accuracy can further be improved by repeating the measurements several times. This allows to determine the general trend of a series well within ±5%.

Comparison with Theory: For a direct comparison of the measurements with a calculation the key parameters are the temperature sensitivity λ and the fraction f_G of the gas emission absorbed

by the earth plate. While in the absence of a GH-gas λ can directly be deduced from the slope of the measured temperature increase as a function of the electric heating (see Fig. 8), f_G as the ratio of $\Delta H_E/\Delta I_G$ requires a measurement with the individual GH-gases. Unfortunately, can the emitted fraction of a gas not independently be derived only from our measurements, this would require a known volume radiator as reference; the absorbed fraction f_C from the cold plate can only work as a first orientation. Instead, we are using a theoretical reference, the calculated emission of the gas. This allows a direct comparison of ΔH_E with $f_G \cdot \Delta I_G$, as plotted in Figs 10b) - 12b), and from a fit of the theoretical curve to the measured data we finally get f_G.

The good agreement for all three gases with the calculations can be seen for the temperature data as well as for the plate heating (Figs 10 - 12). Particularly the increasing saturation and the characteristic gradation with inclining gas concentration is well confirmed by the calculations and excludes any larger impact by heat conduction. At the same time these graphs demonstrate the only small further impact on global warming with increasing GH-gas concentrations (see, Harde 2017 [29]).

While the coincidence in the absolute values of measured and calculated data is a consequence of using the theoretical reference for deriving f_G as scaling factor for the absorbed back-radiation and also for the temperature plots, is the almost exact agreement of the derived radiative forcing for CO_2 with $\Delta F_{2xCO2} = 3.70$ W/m^2 more an unexpected coincidence with the literature. So, Myhre et al. [28] present a simplified expression for the CO_2 forcing as $\Delta F = \alpha \cdot \ln(C/C_0)$ with $\alpha = 5.35$ W/m^2, which gives a forcing at doubled CO_2-concentration of $\Delta F_{2xCO2} = \alpha \cdot \ln 2 = 3.71$ W/m^2. But this applies for a lot of different conditions in the atmosphere with a significant impact on ΔF_{2xCO2}.

So, a comparable Earth-atmosphere scenario to our measurement would be a surface temperature of T_E = 30°C, a dense cloud cover at about 5,200 m altitude, a CO_2 concentration of 42.7 ppm and no other GH-gases. The cloud cover at this altitude then has a temperature of −11.4°C (slightly increased lapse rate at the higher ground temperature) and radiates with 266 W/m^2 (assuming 100% emissivity), while the reduced CO_2 concentration over a pathlength of 5.2 km ensures a comparable optical path to the experiment (20% ×1.11 m). A simulation under these conditions almost reproduces the measurement with a CO_2 induced back-radiation of 23.5 W/m^2 and a radiative forcing for doubling the concentration from 21.35 ppm to 42.7 ppm of $\Delta F_{2xCO2} = 3.74$ W/m^2. This already includes a first smaller correction due to the declining pressure with altitude, and thus a lower collisional broadening, which reduces the forcing by about 0.2 W/m^2, while the pressure in our measurement and calculation was considered to be constant.

A much larger impact on the back-radiation and the radiative forcing, however, emanates from other GH-gases in the atmosphere, particularly from water vapor. So, under conditions as above and assuming only about one tenth of the regular concentration of H_2O, CH_4 and N_2O, the back-radiation increases by 80 W/m^2, while the CO_2 induced forcing decreases by 1 W/m^2 to 2.71 W/m^2.

When repeating the above calculation with the actual concentrations of the GH-gases (CO_2: 400 ppm; H_2O: 1.46%; CH_4: 1.8 ppm; N_2O: 0.3 ppm), the back-radiation further increases to 418 W/m^2, which is already 87.5% of the up-welling surface emission (478 W/m^2), but due to the strongly overlapping and saturated absorption bands the forcing even reduces to $\Delta F_{2xCO2} = 2.06$ W/m^2. For a ground temperature of 16 °C it further goes down to 1.47 W/m^2 (see Appendix 5, Fig. A5).

A more realistic scenario with a global mean Earth temperature of 16°C, a mean cloud cover of 66%, a cloud emissivity of 63% and calculating the radiative forcing at the top of the atmosphere (TOA) finally gives a value of $\Delta F_{2xCO2} = 3.4$ W/m^2 (see also Appendix 5). So, this must be seen more as a coincidence, when our measurement almost reproduces this measure with its different impacts, which even partly compensate each other. Nevertheless, is this an important orientation, and both the back-radiation by CO_2 and the almost logarithmic variation of the radiative forcing with concentration changes, as expected from the calculations, can well be confirmed by our

measurements. With a Planck response of λ_P = 0.31 °C/(W/m^2), as specified by the IPCC [27] and without feedbacks this gives a basic Equilibrium Climate Sensitivity of $ECS_B = \lambda_P \cdot \Delta F_{2xCO2} \approx$ 1.05°C.

Respective values for CH_4 and N_2O can only indirectly be compared with the literature, as they are only specified for a concentration range (parts per billion) before saturation is observed.

Lineshape Considerations: While standard calculations are using a Lorentzian lineshape for the individual collision broadened transitions, some deviation is expected when assuming a different profile. Measurements by Edwards and Strow [30] on bands of CO_2, e.g., suggest that the far wings decrease approximately exponentially with detuning from the line center, while Lorentz profiles give too much absorption for larger detunings. The reason is that Lorentzian lineshapes result from assuming an infinitely short collision duration between molecules, but in reality collisions typically take a few ps (see also Wijngaarden & Happer, 2020 [31]).

Such a modified shape can be expressed by a core profile, which is multiplied by a wing-suppression factor. To assess the influence of a reduced wing absorption and thus also a reduced back-radiation we have performed LBL-RT calculations with a Lorentzian core profile and a sech^2-wing-suppression function:

$$g_{L,\mathrm{mod}}(\tilde{\nu}) = \frac{\Delta\tilde{\nu}_{mn}/2\pi}{(\tilde{\nu}-\tilde{\nu}_{mn})^2 + (\Delta\tilde{\nu}_{mn}/2)^2} \cdot \left\{ \frac{2}{e^{(\tilde{\nu}-\tilde{\nu}_{mn})/\Delta\tilde{\nu}_s} + e^{-(\tilde{\nu}-\tilde{\nu}_{mn})/\Delta\tilde{\nu}_s}} \right\}^2, \qquad (15)$$

with $\tilde{\nu}_{mn}$ as the transition wavenumber, $\Delta\tilde{\nu}_{mn}$ as the full linewidth caused by collisions (FWHM) and $\Delta\tilde{\nu}_S$ as detuning, at which the wings are declining to 0.42 of their original value.

We use a detuning parameter of $\Delta\tilde{\nu}_S = 10 \cdot \Delta\tilde{\nu}_{mn}$, which for $\Delta\tilde{\nu}_{mn} \approx 0.18\,\mathrm{cm}^{-1}$ corresponds to a detuning of $\Delta\tilde{\nu}_S \approx 1.8\,\mathrm{cm}^{-1}$ and a collision time of a few ps. With the reduced wings also the calculated gas emission ΔI_G is declining, and thus gives a larger f_G to fit the measurements. But a larger f_G finally results in a smaller radiative forcing compared to a pure Lorentzian shape. Table 3 displays a comparison without and with wing-suppression. The radiative forcing for CO_2 and N_2O reduces by about 10%, for CH_4 even by 20%.

Table 3: Comparison of radiative forcings without and with wing-suppression for CO_2, CH_4 and N_2O.

RF (W/m^2)	no wing suppression	with wing suppression
ΔF_{2xCO2}	3.70	3.4
ΔF_{2xCH4}	2.75	2.2
ΔF_{2xN2O}	5.00	4.5

We note that the values in Table 3 were derived from a logarithmic fit to the temperature data to directly compare the radiative forcings of these gases at doubled concentration. Despite the significantly different concentrations of these gases in the atmosphere with differences of more than a factor of 1,000 and thus with a different inset of saturation effects, the radiative forcings are an appropriate means to characterize the gases in terms of their radiative properties. So, we see that individual CH_4 molecules only contribute 65% relative to CO_2 molecules and less than 50% relative to N_2O molecules to the GHE under otherwise same conditions. This also holds in good approximation when considering the gases at considerably lower concentrations before saturation is dominant (see, Harde 2021 [32]).

In this context we have to point to an often-found misinterpretation concerning the global warming potential of methane. So, the radiative efficiency of CH_4 with 3.7x10^{-4} W/m^2/ppb is classified to be 25x larger than that of CO_2 with 1.4x10^{-5} W/m^2/ppb. Such values are derived from the changing absorptivity or emissivity of the gases, when their concentration is changing by 1ppb (parts per billion). But what is done in this case is to compare two gases under completely different conditions: CH_4 at a concentration of 1.8 ppm and CO_2 at a 200x larger concentration, when

it is already strongly saturated. Also, the interference with other green-house gases, particularly with water vapor, is for both gases completely different. Only these diverse conditions pretend a much higher radiative efficiency of methane, respectively a considerably lower value for CO_2. So, at a concentration of 400 ppm in the atmosphere or at 10% in the laboratory experiment the radiative efficiency of CH_4 drops to about 60% of CO_2 (see Table 3), and at a concentration of 1.8 ppm the efficiency of CO_2 is about 1.5 times larger than for CH_4 (see also Wijngaarden & Happer 2019 [33]). Only due to the different saturation strengths on quite different scales is CH_4 assumed to have a 25x larger global warming potential, while a more realistic consideration supposing a doubling each of the actual CH_4, N_2O and CO_2 concentrations shows that CH_4 does not contribute more than about 2% to global warming (Harde 2021 [32]) and N_2O only about 1% relative to CO_2.

7. Conclusion

To our knowledge we present the first demonstration of the atmospheric greenhouse effect in a laboratory experiment, which also allows quantitative measurements under conditions as in the lower troposphere. We use an experimental set-up consisting of two plates in a closed housing, one plate in the upper position heated to 30°C, the other at the bottom and cooled to -11.4°C. The plates have a distance of 1.11 m to each other, and the tank can be filled with the gases of interest to study the radiation transfer between the plates. This set-up largely eliminates convection or heat conduction and allows to reproducibly study the emission of the GH-gases as additional warming of the heated plate due to back-radiation of the gases. We have investigated the GH-gases carbon dioxide, methane and nitrous oxide as a function of the gas concentration. In addition, and independent of the temperature measurements is the back radiations of the GH gases directly recorded as reduced electrical heating of the upper plate.

These measurements clearly demonstrate that contrary to the often misinterpreted 2nd law of thermodynamics a warmer body can further be heated by absorbing the radiation from a colder body, here the radiation from the cooled plate and a GH-gas. The measurements are well confirmed by extensive LBL-RT calculations, which are in full agreement with the recorded temperature and electric heating data, this in absolute numbers and over the whole progression as a function of the gas concentrations. Any noticeable impact in the energy balance due to heat conduction can be excluded by control experiments with noble gases.

At the same time reveal our theoretical studies the principal difficulties to measure the GH-effect as increasing temperature of the gas. More careful examination shows that such trials simply demonstrate heating via absorption of IR or NIR light by the compartment walls, only to some smaller degree by absorption of a gas. But these experiments miss that the greenhouse effect is mainly the result of a temperature difference over the propagation path of the radiation and thus the lapse rate in the atmosphere. A declining GHE with reduced temperature difference between the plates is clearly demonstrated. And *it is an interesting curiosity that, had convection produced a uniform temperature, there wouldn't be a greenhouse effect* (Lindzen 2018 [34]).

Simply expressed: the greenhouse effect contributes to some warming of the Earth's surface and by this also to some additional convection, but not to any remarkable direct warming of the air temperature. At least that is the lesson learned from the experiments with CO_2, methane and nitrous oxide. This finding is of particular importance since air warming is a necessary prerequisite for the alleged CO_2-water vapor feedback, without which there would be no threatening Earth warming.

From our measurements and their comparison with the calculations we derive the radiative forcing of the gases when doubling their concentrations. This is an important measure to characterise the emissivity of the gases under higher concentration levels, when already stronger saturation on the absorption bands is observed, but it also serves as a relative measure at lower concentrations. The found forcings are in good agreement with literature values, which to some degree is also the

result of calibrating the set-up to the spectral calculations based on the HITRAN database, but which independently determine the impact of the gases as a function of their concentration.

While standard calculations for such comparison are using a Lorentzian lineshape for the individual collision broadened transitions, measurements on absorption bands of CO_2 suggest that the far wings decrease approximately exponentially with detuning from the line center, and thus are contributing less absorption for larger detunings than Lorentz profiles. Therefore, we have performed additional calculations with a sech^2-wing-suppression profile, and under our experimental conditions we find for the radiative forcing of CO_2 at doubled concentration: $\Delta F_{2xCO2} = 3.4$ W/m^2, for CH_4: $\Delta F_{2xCH4} = 2.2$ W/m^2 and for N_2O: $\Delta F_{2xN2O} = 4.5$ W/m^2. These values are for CO_2 and N_2O about 10% and for CH_4 20% lower than the standard values.

Water vapor as the by far strongest GH-gas in the atmosphere could not be investigated in our set-up. This would require some systematic modifications to realize a similar vapor density profile over the lapse rate as in the atmosphere, and in particular, to avoid condensation at the cold plate. But it would be highly desirable to realize also for this GH-gas quantitative measurements, together with CO_2 as a mixture, to study the interdependence of these gases in their overlapping absorption spectra and by this to collect more reliable data about their impact on our climate. Based on a set-up as presented here but with a further developed equipment, particularly with well stabilized components and an improved temperature recording such investigations would be very helpful for objectification of the further climate debate.

Already the presented measurements and calculations demonstrate the only small impact on global warming with increasing GH-gas concentrations due to the strong saturation. Therefore, we strongly recommend not to further provoke crying and jumping kids by fake experiments and videos only to generate panic, but to teach them in serious science with realistic demonstrations and information about the impact and also benefits of GH-gases. Then scholars and also adults can decide, if it is worthwhile to further demonstrate on streets for a stable climate, which apparently is mainly controlled by natural impacts (see Harde & Salby 2021 [35]; Salby & Harde 2021 [36, 37]), and if we are really living on a planet, which can only be rescued by stopping all fossil fuel emissions without a realistic perspective for a secure and healthy future of our lives. In the long term, an economic shift to new forms of energy generation, of whatever kind, is inevitable, since the supply of fossil fuels is finite. However, there is no need to drive this process blindly and hastily; otherwise, there is a risk of deindustrialization, which would then really trigger a dire future for the next generations.

Funding

This research did not receive any specific grant from funding agencies in the public, commercial, or not-for-profit sectors. The experimental set-up was developed and paid privately by MS.

Guest-Editor: Prof. Jan-Erik Solheim; Reviewers were anonymous.

Acknowledgements

We thank Eike Roth and Christoph Marvan for stimulating discussions and valuable advices. Also, we thank Ulrich Tengler for his support with a cryostat. Further we would like to express our special thanks to the editors and reviewers for their comments and support of this publication.

Appendix 1 - Experimental Set-Up

The main components of the experimental setup consist of the tank, the earth plate, the cold plate, and the upper dome (Fig. 1). The earth plate is a composite of a 0.8 mm thick blackened aluminum disk (Ø = 16.7 cm) with an equally sized self-adhesive heating foil (12 V/DC, AC 14 W) on its back side. As insulation between the heating foil and upper dome works a 2 cm thick Styrofoam

disc (Ø = 17 cm) which is glued to the dome (Fig. A1.1a).

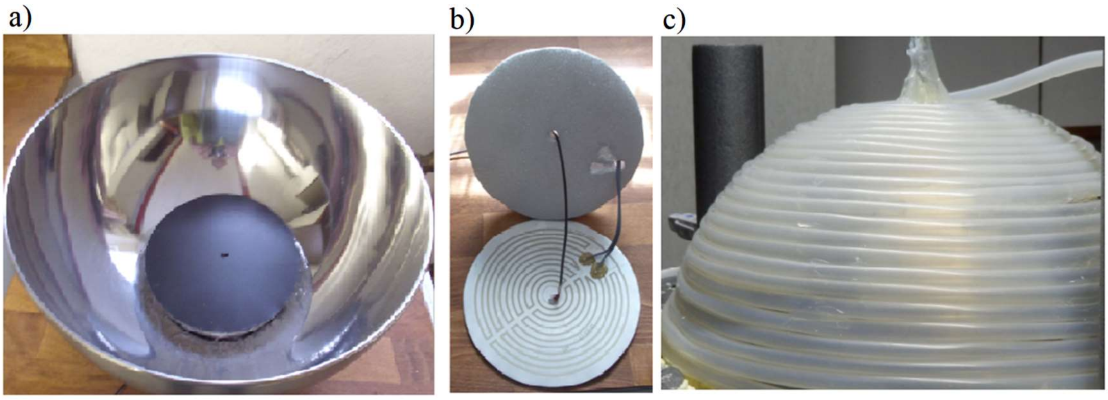


Figure A1.1: a) Earth plate with temperature sensor in the upper dome, b) Back side of the earth plate with heating foil and polystyrene disc, c) Outside of the dome with vinyl tubing for the thermostated water. In the background one of the 23 pipe insulations, made of flexible polyethylene foam for the tank and dome insulation.

The temperatures of the earth plate, the upper dome and the cold plate are measured by temperature sensitive diodes (Infineon KTY 11-5: TO-92) and are recorded every 3 minutes by a computer. The calibration is described in Appendix 2.

The earth plate heating is supplied by a digital laboratory power device (KA3005D, 0 – 15 V, resolution 0.01 V) in constant voltage mode. The heating power is the voltage times current for the earth plate of 219.04 cm^2. This value is multiplied by 45,654 to convert to an area of 1 m^2 (H_{PE}).

For a temperature increase δT_E of 0.13°C the voltage must be changed by 0.03 V. The accuracy of the temperature reading of the earth plate is ± 0.13°C, which is our limit of detection. Due to this digital display two heating values, an upper and a lower value, are recorded at intervals of 0.01 V and their average determines the temperature T_E (Appendix 4, Table A4.1).

The upper dome is wrapped with a vinyl tube (Ø = 10 mm) through which thermostated water flows (ESCO ES 10) with a temperature of 30.0 ± 0.1°C (Fig. A1.1c). The free space above the dome is filled with Styrofoam flakes and sealed with a 5 cm thick Styrofoam disc.

The tank consists of two 0.8 mm thick, 1 x 1 m aluminum sheets bonded with silicone (Fig. A1.2a). The inside is polished and the two seams are covered with aluminum foils (Fig. A1.2b). From the outside, the tank is wrapped in three sections, each with 25 m (Ø =12 mm) PVC tubing, through which thermostated water flows, only for calibration of the temperature sensors (Fig. A1.2c). For all other measurements, the water is removed from the PVC hoses.

In distances of 25 cm the tank has 3 small holes and one hole in the upper dome to place thermometers (TFA 30.1040) 2 cm deep, which measure the wall temperatures T_1 to T_4 at these positions. Since all measurements are made at thermal equilibrium, it is assumed that the air in the tank has approximately the same temperature as the wall at that position.

The cold plate in the lower dome consists of a 0.6 mm thick copper disk (Ø = 35.5 cm) with a diode (Infineon KTY 11-5: TO-92) and 5 thermocouples (TEC1-12706, 40 x 40 x 3.8 mm) mounted in the center (Fig. A1.3a). The voltage of the thermocouples is measured with a digital multimeter (HP-760D) and indicates the injection of heavy sample gases in the lower dome by a voltage drop.

A 6 m long (Ø = 8 mm) copper tube is soft soldered to the back of the cold plate, through which an ethanol-water mixture flows, which can be cooled down to -16 °C by a cryostat (Isotemp

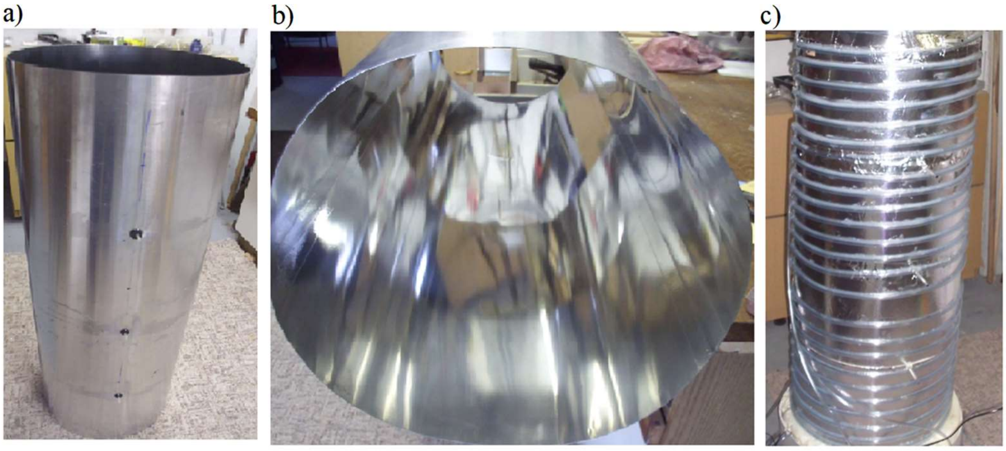


Figure A1.2: a) Exterior view of the tank with the rubber discs for placing thermometers, b) Interior view of the polished Al-tank, c) PVC hoses for temperature control of the tank.

1016S). The copper tubes are thermally insulated with urethane construction foam and the insulation layer sealed with bottom paint.

To insulate the tank and the two domes, 23 polyethylene soft foam pipe insulations (5 x 140 cm) are glued to the pipe wall, the interiors are filled with 1 mm polystyrene balls and wrapped with 7 layers of aluminum-laminated polystyrene wallpaper, creating a 7 cm thick insulation layer. The room temperature is thermostated (ESCO ES 10) to 20.5 ± 0.2°C by a fan heater and two additional fans.



Figure A1.3: a) Cold plate with 5 thermocouples and temperature sensor in the lower dome, b) Back side of the cooling plate with copper spiral connected to the cryostat, c) Polyurethane insulation of the copper spiral.

Prior to each measurement, the air in the tank is pumped around for 12 hours with a flow rate of 1.5 l/min over solid sodium hydroxide, minimizing water vapor and CO_2 concentrations in the air (Fig. 1). The sodium hydroxide container is then removed directly before starting a run. 6 - 8 hours earlier the room thermostat, the heater for the earth plate and the cryostat for the cold plate are switched on to stabilize the set-up at the desired temperatures.

The IR-active gases CO_2, CH_4 and N_2O are stored in small gas bottles or cans and the respective quantities are determined by weighing. The volumes of helium and argon are metered via a rotameter (Brooks instrument 0 - 3.5 l/min). The gases are injected through 10 cm long copper tubes (Ø = 6 mm) either into the lower dome below the cold plate or into the upper dome below the earth plate, depending on their specific density compared to air (Fig. 1). An air pump then sucks the air out of the upper dome and fills it back into the lower inlet to mix the air and gas evenly. The measurement of the oxygen concentration (Sumatec technical diving) ensures that air and sample gases have been completely homogenized (Fig. 1). For the purity of the sample gases see Table A1.

Table A1: Origin and purity of the sample gases

Gas	Distribution	Purity (%)
CO_2	Cosmeda	99.9
CH_4	WINDAUS-Labortechnik	99.9
N_2O	LG Engros ApS	99.7
Ar	Hornbach	99.9
He	Amazon	99.9

Appendix 2 - Calibration of the Temperature Sensors

The calibration of the temperature sensor (diode) for the earth plate (T_E) and the thermometers (T_1 - T_2) is carried out by gradually heating the entire apparatus from 20 to 34°C (Fig. A2a) . For this purpose, water at a defined temperature (from a water thermostat (ESCO ES 10) with a calibrated thermometer GDR, TGL 11996 N, 0.2 K) is pumped simultaneously through the pipes of the cooling plate (Fig. A1.3a), the tank (Fig. A1.2c) and the dome (Fig. A1.1c). The recorded signals are correlated with the water temperatures. The absolute temperature of the earth plate can deviate from the specified values by up to 0.2 °C due to the limited accuracy of the calibration thermometer.

a) b)

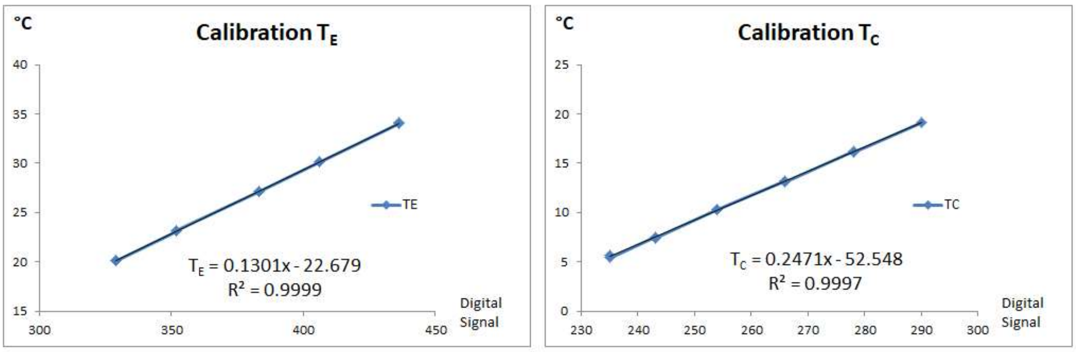


Figure A2: Calibration of the temperature sensors, a) Temperature of the earth plate T_E, b) Temperature of the cold plate T_C.

The calibration of the cold plate diode (T_C) and the thermometers (T_3 - T_4) is performed in the same way except that instead of a thermostat, the Isotemp 1016S cryostat is connected and the water temperature is gradually cooled from 20 to 5°C (Fig. A2b). When the water temperature is further reduced, larger heat losses occur and the linear trend is no longer given. Therefore, a temperature measurement $T_C < 5$°C is done by extrapolation with a linear trend according to Fig. A2b). The absolute temperature of the cold plate can deviate from the specified values by up to 0.2 °C due to the limited accuracy of the calibration thermometer.

Appendix 3 - Influence of Heat Conduction

When the tank is filled with a sample gas, as described in Subsec. 5.1 to 5.3, the heat conductivity $L(\Delta T)$ of the gas mixture changes as a function of temperature and gas concentration, since air and sample gas have different thermal conductivities (Table A3). This could change the heat transport and according to eq. (8), $K(T_W, \Delta T)$ as well as the temperature of the earth plate T_E could change.

Table A3: Heat conductivity of air and sample gases

Gas	Heat Conductivity 25 °C κ (W/m·K)
CO_2	0.016
N_2O	0.017
Ar	0.018
Air	0.026
CH_4	0.034
He	0.150

Such objection can be checked by control experiments with the noble gases Ar and He (Fig. A3), which are IR-inactive but have different thermal conductivities compared to air (Table A3). The measurements with these gases were performed under identical experimental conditions as described in Subsec. 5.1 and with concentrations of 10% and 20%, respectively.

a)

b)

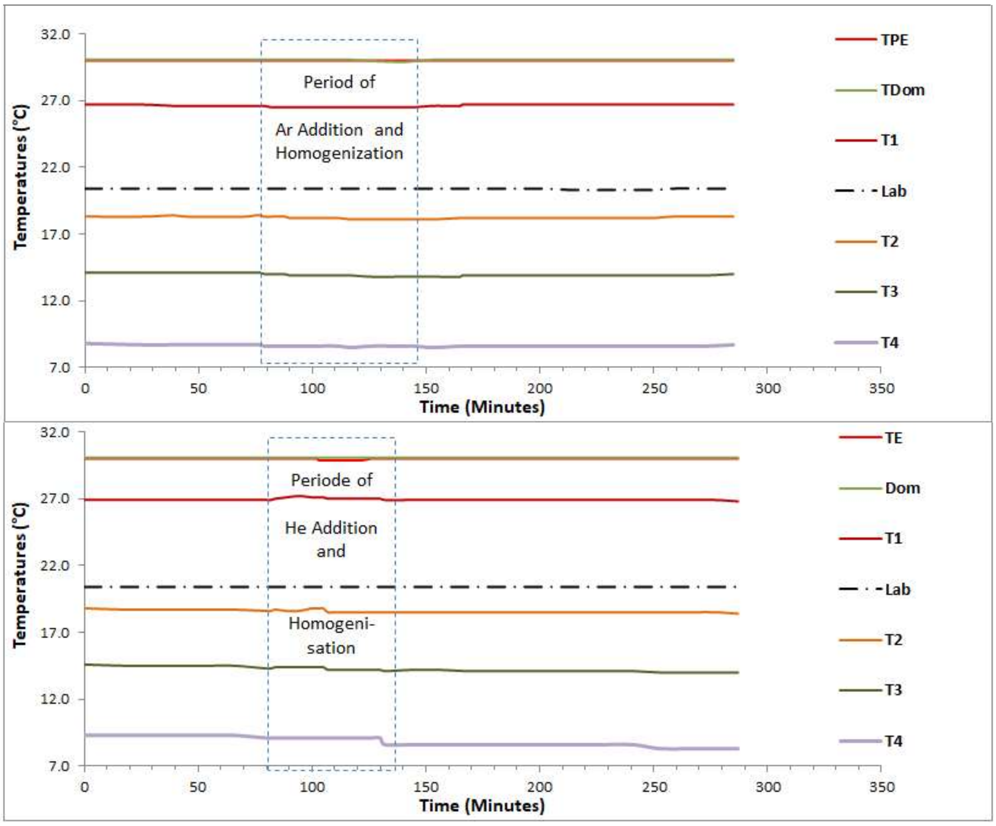


Figure A3: a) Control test with 10% Ar and b) with 20% He. Plotted are the temperatures of the earth plate (Red), the dome (Green), the gas temperature at 4 positions (T_1 - T_4) and the laboratory temperature (Black).

None of these trials showed any change of the earth plate temperature T_E. This is not really surprising, because already the cooling experiments with the noble gases in Sec. 4 (see also Appendix 4, Table A4.3) had no influence, although the temperatures were changing over a much wider range.

Appendix 4 - Details for the Validation of the Measuring System (Section 4)

In this appendix we have compiled typical data for the cooling experiment of Subsec. 4.1 when changing the temperature T_C of the cold plate between -12.9°C and +10.9°C (Table A4.1, column

2) while measuring the electric heating intensity H_E for the earth plate (column 3) to stabilize the temperature T_E of the earth plate at 30°C (column 1). Due to the thermal inertia of the measuring system, two values for H_E are always recorded for one temperature step.

Table A4.1: Example of a cooling experiment; T_C from -12.9°C up to +10.9°C

T_E °C	T_C °C	H_E W/m²	I_E W/m²	I_C W/m²	ΔT °C	I_E-I_C W/m²	Room T_p °C
30.0	-12.9	169.6	478.9	260.3	42.9	218.6	20.3
30.0	-12.9	169.9	478.9	260.3	42.9	218.6	20.3
30.0	-7.2	153.9	478.9	283.6	37.2	195.3	20.4
30.0	-7.2	152.8	478.9	283.6	37.2	195.3	20.4
30.0	-1.1	133.9	478.9	310.6	31.1	168.3	20.4
30.0	-1.1	133.7	478.9	310.6	31.1	168.3	20.4
30.0	5.3	111.9	478.9	340.7	24.7	138.2	20.4
30.0	5.3	111.3	478.9	340.7	24.7	138.2	20.4
30.0	10.9	90.5	478.9	369.0	19.1	109.9	20.3
30.0	10.9	89.7	478.9	369.1	19.1	109.8	20.3

Table A4.2: $f_C = \Delta H_E/\Delta I_C$ and $H_E(0,T_W)$ in air; T_C from -13°C to +11°C, T_E = 30°C

No.	$\Delta H_E/\Delta I_C$	$H_E(I_C$=0)
1	0.73	361.4
2	0.75	366.1
3	0.74	363.7
4	0.74	362.5
5	0.75	365.6
6	0.74	361.8
7	0.74	363.9
8	0.75	366.1
9	0.75	366.8
10	0.74	363.5
Ø	0.74	364.1
Std Dev.	0.005	1.8

The repeatability and accuracy of such measurements is demonstrated by a series of 10 independent runs (see Table A4.2). These data are compared with the difference of the calculated intensity I_E of the earth plate as loss and the emitted intensity I_C of the cold plate as maximum possible radiation, which can be absorbed by the earth plate to partially compensate for the losses. According to eq.(7) from these data we derive the fraction f_C of the cold plate radiation, which is absorbed by the earth plate (see Fig. 6).

Table A4.3 displays identical measurements only with different sample gases.

Table A4.3: Slope $\Delta H_E/\Delta I_C$ and $H_E(0,T_W)$ with sample gases; T_C from -13°C to +11°C, T_E = 30°C

Gas	C Vol.-%	$\Delta H_E/\Delta I_C$	$H_E(I_C$=0) (W/m²)
Ar	10	0.73	362
Ar	20	0.75	367
He	10	0.74	365
He	20	0.74	362
CH_4	10	0.70	345
CO_2	10	0.68	335
N_2O	10	0.66	324

Appendix 5 - Different Impacts on Radiative Forcing

To assess the different contributions, which mainly modify the radiative forcing under atmospheric conditions and also determine the difference to our measurement, we start with conditions comparable to the experiment and then adapt them step by step to the atmospheric situation to evaluate their individual impacts on ΔF_{2xCO2}.

For a ground temperature T_E = 30°C and a cloud cover at 5.2 km altitude the optical path through a dry atmosphere with a CO_2 concentration of 42.69 ppm would be the same as for a 20% CO_2 concentration in air over a distance of 111 cm. At this altitude the clouds have a temperature of −11.4°C and are supposed to emit like a black body. A simulation under these conditions gives a forcing of ΔF_{2xCO2} = 3.74 W/m^2 and almost exactly reproduces the laboratory experiment, but already includes a first correction due to the declining pressure with altitude. This contributes to a lower collisional broadening and reduces the forcing by 0.22 W/m^2, while with a constant pressure in the tank this gives a theoretical forcing of 3.96 W/m^2 (see below). Fig. A5 reveals the individual changes of the forcing as up or down directed arrows in W/m^2.

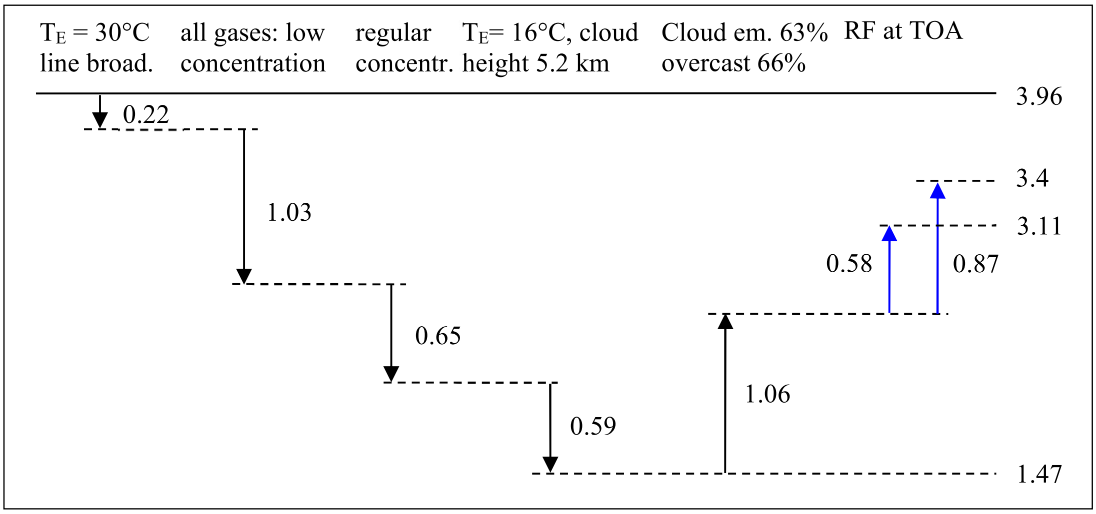


Figure A5: Changes of radiative forcing ΔF_{2xCO2} in W/m$_2$ caused by different impacts. Black arrows indicate changes in the back-radiation, blue arrows in forward radiation (to TOA).

A significantly stronger impact emanates from other GH-gases in the atmosphere, particularly from water vapor. Assuming only about one tenth of the regular concentration of H_2O, CH_4 and N_2O, the back-radiation already increases by 80 W/m^2 (from 289.5 to 369.0 W/m^2), while the CO_2 induced forcing decreases by 1.03 W/m^2 to 2.71 W/m^2.

When supposing regular concentrations in the atmosphere with 400 ppm CO_2, without other GH-gases the forcing would jump up to 5.7 W/m^2 (not shown), but in the presence of the other gases at normal concentrations (H_2O: 1.46%; CH_4: 1.8 ppm; N_2O: 0.3 ppm) the forcing further declines. While the back-radiation increases to 418 W/m^2, which is already 87.5% of the up-welling surface emission (478 W/m^2), owing to the strongly overlapping and saturated absorption bands the forcing even declines by additional 0.65 W/m^2 to ΔF_{2xCO2} = 2.06 W/m^2.

A further decrease by 0.59 W/m^2 to 1.47 W/m^2 is expected when lowering the ground temperature to 16°C at otherwise same conditions. On the other hand, semitransparent clouds with an emissivity of 0.63 and an overcast of 66% increase the forcing by 1.06 W/m^2 to 2.53 W/m^2, which is just 64% of the initial value.

However, direct comparison with literature often requires to consider the forcing in upward direction from the surface to TOA, which due the longer interaction over the whole atmosphere and with varying O_3 concentration over the stratosphere further raises the forcing by 0.58 W/m^2 to ΔF_{2xCO2} = 3.11 W/m^2 (left Blue Arrow in Fig. A5). Different to this more straight forward

calculation other approaches consider the forcing as difference of the upwelling and downwelling sw and lw radiation in the tropopause, while simultaneously assuming stratospheric thermalization (Myhre et al. [28]). These different attempts rely on the applied models used to calculate the global warming caused by the GH-gases, and therefore they also differ in their size.

We note that the calculated forcings at doubled CO_2 concentration not strictly obey a logarithmic dependency but show relatively higher values for higher concentrations. E.g., a calculation for 200 ppm doubled gives a forcing 0.4 W/m^2 larger than the respective calculation for 100 ppm. While our experimentally derived value with ΔF_{2xCO2} = 3.7 W/m^2 was determined by a fit to the measured data over a wide range from 1.25% up to 20% (16x), only doubling from 10% to 20% gives a value of 3.96 W/m^2. This also explains the higher start value in Fig. A5, and all other forcings or changes in this subsection, which relate to this figure were found by doubling 21.35 ppm resp. 200 ppm.

All black arrows in Fig. A5 designate changes in the back-radiation, whereas blue arrows indicate the difference to a calculated upward forcing at the TOA. In this case is the upward forcing 0.58 W/m^2 larger than the downward forcing. And when calculating the doubling with an initial concentration as assumed in pre-industrial times with 280 ppm, this gives a final radiative forcing at TOA of ΔF_{2xCO2} = 3.4 W/m^2.

References

1. J. B. Fourier, 1824: *Remarques Générales Sur Les Températures Du Globe Terrestre Et Des Espaces Planétaires*. In: *Annales de Chimie et de Physique*, Vol. 27, 1824, S. 136–167. https://books.google.co.uk/books?id=1Jg5AAAAcAAJ&pg=PA136&hl=pt-BR&source=gbs_selected_pages#v=onepage&q&f=false, Oct.21
2. J. Tyndall, 1861: *On the Absorption and Radiation of Heat by Gases and Vapours, and on the Physical Connexion of Radiation, Absorption, Conduction*, The Bakerian Lecture, The London, Edinburgh, and Dublin Philosophical Magazine and Journal of Science, Series 4, Vol. 22, https://www.jstor.org/stable/108724, Oct.21
3. G. Kirchhoff, 1859: *Monatsberichte der Akademie der Wissenschaften zu Berlin*, Sessions of Dec. 1859, 1860, Berlin, pp. 783-787).
4. J. Stefan, 1879: *Über die Beziehung zwischen der Wärmestrahlung und der Temperatur*, in: Sitzungsberichte der mathematisch-naturwissenschaftlichen Classe der kaiserlichen Akademie der Wissenschaften, Bd. 79 (Wien 1879), pp. 391-428.
5. L. Boltzmann, 1884: *Ableitung des Stefan'schen Gesetzes, betreffend die Abhängigkeit der Wärmestrahlung von der Temperatur aus der electromagnetischen Lichttheorie*, Annalen der Physik und Chemie. Bd. 22, pp. 291–294, https://doi.org/10.1002/andp.18842580616.
6. M. Planck, 1900: *Zur Theorie des Gesetzes der Energieverteilung im Normalspectrum*, Verh. Deutsche Phy. Gesell. 2, No. 17, p. 220 and pp. 237-245.
7. S. Arrhenius, 1896: *On the influence of carbonic acid in the air upon the temperature of the ground*. In: Philosophical Magazine and Journal of Science. Vol. 41, No. 251, April 1896, S. 237-276, https://doi.org/10.1080/14786449608620846, Oct.21
8. R. W. Wood, 1909: *Note on the Theory of the Greenhouse*, London, Edinborough and Dublin Philosophical Magazine, Vol. 17, pp. 319-320.
9. N. S. Nahle, 2011: *Repeatability of Professor Robert W. Wood's 1909 experiment on the Theory of the Greenhouse,* Biology Cabinet Online-Academic Resources and Principia Scientific International, Monterrey, N. L.
10. V. R. Pratt, 2020: *Wood's 1909 greenhouse experiment, performed more carefully*, http://clim.stanford.edu/WoodExpt/, Dec. 2021.

11. E. Loock, 2008: *Der Treibhauseffekt - Messungen an einem Wood'schen Treibhaus*, https://docplayer.org/30841290-Der-treibhauseffekt-messungen-an-einem-wood-schen-treibhaus-von-ehrenfried-loock-version.html, Oct.21.

12. T. O. Seim, B. T. Olsen, 2020: *The Influence of IR Absorption and Backscatter Radiation from CO_2 on Air Temperature during Heating in a Simulated Earth/Atmosphere Experiment*, Atmospheric and Climate Sciences, 10, pp. 168-185, https://doi.org/10.4236/acs.2020.102009, Oct.21.

13. H. v. Ditfurth, 1978: *Treibhauseffekt*, https://www.youtube.com/watch?v=lORAR1nvfjs, Oct.21.

14. M. Schnell, 2020: *Die falschen Klimaexperimente*, https://www.eike-klima-energie.eu/2020/11/06/die-falschen-klima-experimente/, Oct.21

15. A. Gore, D. Guggenheim, 2006: *An Inconvenient Truth*, Movie, https://www.imdb.com/title/tt0497116/, Oct.21

16. A. Watts, 2011: *Replicating Al Gore's Climate 101 video experiment shows that his "high school physics" could never work as advertised*, https://wattsupwiththat.com/2011/10/18/replicating-al-gores-climate-101-video-experiment-shows-that-his-high-school-physics-could-never-work-as-advertised/?cn-reloaded=1, Oct.21

17. J.-E. Solheim, 2016: *Start des zweitägigen „Al Gore-Experiments"*, 10. Internationale Klima- und Energie-Konferenz (10. IKEK), EIKE, Berlin, https://www.eike-klima-energie.eu/2017/02/04/10-ikek-prof-em-jan-erik-solheim-start-des-zweitaegigen-al-gore-experiments/, October 2021

18. L. S. Rothman, I. E. Gordon, A. Barbe et al., 2009: *The HITRAN 2008 molecular spectroscopic database*, J. Quantitative Spectroscopy and Radiative Transfer, vol. 110, no. 9-10, pp. 533–572.

19. H. Harde, 2013: *Radiation and Heat Transfer in the Atmosphere: A Comprehensive Approach on a Molecular Basis*, Intern. Journal of Atmospheric Sciences, vol. 2013, Article ID 503727, 26 pages, http://dx.doi.org/10.1155/2013/503727, Oct.21.

20. H. Harde, J. Pfuhl, 2016: *MolExplorer - A Program-Platform for the Calculation of Molecular Spectra and Radiation Transfer in the Atmosphere*, Helmut-Schmidt-University Hamburg, http://hharde.de/#xl_xr_page_research%20j, Oct.21.

21. K. Schwarzschild, 1906: *Über das Gleichgewicht der Sonnenatmosphäre*. In: Nachrichten von der Königlichen Gesellschaft der Wissenschaften zu Göttingen, Mathematisch-Physikalische Klasse, 1906, Heft 1, pp. 41–53 (13. Januar 1906).

22. M. Wolff, H. Harde, 2003: *Photoacoustic Spectrometer Based on a Planckian Radiator with Fast Time Response*, Infrared Physics and Technology 44, pp. 51-55.

23. H. Harde, G. Helmrich, M. Wolff, 2010: *Opto-Acoustic ^{13}C-Breath Test Analyzer,* BIOS, Proc. SPIE 7564, Photons Plus Ultrasound: Imaging and Sensing 2010, 75641E (24 Feb. 2010), San Francisco, https://doi.org/10.1117/12.841660, Oct21.

24. D. Tobin, 1986: *Data Courtesy of D. Tobin*, Space Science and Engineering Center, University of Wisconsin-Madison, Madison, USA.

25. P. Arnott, 2008: *Graphic from Pat Arnott*, University of Nevada, Reno, USA, ATMS 749

26. D. R. Feldman, W. D. Collins, P. J. Gero, M. S. Torn, E. J. Mlawer, T. R. Shipert, 2015: *Observational determination of surface radiative forcing by CO_2 from 2000 to 2010,* Nature 519, No. 7543, p. 339. https://doi.org/10.1038/nature14240, Oct21.

27. Sixth Assessment Report (AR6) of the IPCC, 2021: *Summary for Policymakers*. In: Climate Change 2021: The Physical Science Basis. Contribution of Working Group I to the Sixth

Assessment Report of the Intergovernmental Panel on Climate Change [Masson-Delmotte, V. et al. (eds.)]. Cambridge University Press.

28. G. Myhre, E. J. Highwood, K. P. Shine, and F. Stordal, 1998: *New estimates of radiative forcing due to well mixed greenhouse gases*," Geophysical Research Letters, vol. 25, no. 14, pp. 2715–2718.

29. H. Harde, 2017: *Radiation Transfer Calculations and Assessment of Global Warming by CO_2*, International Journal of Atmospheric Sciences, Volume 2017, Article ID 9251034, pp. 1-30, https://doi.org/10.1155/2017/9251034, https://www.hindawi.com/journals/ijas/2017/9251034/, Oct21.

30. D. P. Edwards, L. L. Strow, 1991: *Spectral Lineshape Considerations for limb Temperature Sounders*, J. Geophys. Res. 96, p. 20859.

31. W. A. van Wijngaarden, W. Happer, 2020: *Dependence of Earth's Thermal Radiation on Five Most Abundant Greenhouse Gases,* arXiv.org > physics > arXiv:2006.03098 https://arxiv.org/pdf/2006.03098.pdf, Oct21.

32. H. Harde, 2021: *Methane Sensitivity*, http://hharde.de/#xl_xr_page_climate%20b, Oct21.

33. W. A. van Wijngaarden, W. Happer, 2019: *Methane and Climate*, https://co2coalition.org/wp-content/uploads/2021/08/Methane-and-Climate.pdf, Oct21.

34. R. Lindzen, 2018: *The 2018 Annual GWPF Lecture: Global Warming for the Two Cultures,* The GlobalWarming Policy Foundation, 2018 Annual GWPF Lecture, Institution of Mechanical Engineers, London, 8 October 2018, https://www.thegwpf.org, Oct21.

35. H. Harde and M. L. Salby, 2021: *What Controls the Atmospheric CO_2 Level*?, Science of Climate Change, Vol. 1, No. 1, pp. 54-69, https://doi.org/10.53234/scc202106/22, Oct21.

36. M. L. Salby, H. Harde, 2021: *Control of Atmospheric CO_2 - Part I: Relation of Carbon 14 to Removal of CO_2*, Science of Climate Change, Vol. 1, No.2, pp. 177-195, https://doi.org/10.53234/scc202112/30.

37. M. L. Salby, H. Harde, 2021: *Control of Atmospheric CO_2 - Part II: Influence of Tropical Warming*, Science of Climate Change, Vol. 1, No.2, pp. 196-212, https://doi.org/10.53234/scc202112/12.